Sedimentary Geology 443 (2023) 106301

Contents lists available at ScienceDirect

Sedimentary Geology

journal homepage: www.elsevier.com/locate/sedgeo

# Tracking depositional and geochemical variations in the Cambrian North China Platform: Insights from sedimentology, geochemistry, and C-O isotopic records

Muhammad Riaz [a,b,c], Arman Jafarian [d], Ardiansyah Koeshidayatullah [e], Fabrizio Frontalini [f], Lei Jiang [g], Khalid Latif [h], Tehseen Zafar [i,j,*]

[a] State Key Laboratory of Oil and Gas Reservoir Geology and Exploitation, Chengdu University of Technology, Chengdu 610059, China
[b] College of Energy Resources, Chengdu University of Technology, Chengdu 610059, China
[c] Hydrocarbon Development Institute of Pakistan, Islamabad, Pakistan
[d] State Key Laboratory of Biogeology and Environmental Geology, China University of Geosciences, Beijing 100083, China
[e] Department of Geosciences, College of Petroleum Engineering and Geosciences, King Fahd University of Petroleum and Minerals, Dhahran 31261, Saudi Arabia
[f] Dipartimento di Scienze Pure e Applicate (DiSPeA), Università degli Studi di Urbino "Carlo Bo", Campus Scientifico, Località Crocicchia, Urbino 61029, Italy
[g] Key Laboratory of Petroleum Resources Research, Institute of Geology and Geophysics, Chinese Academy of Sciences, Beijing 100029, China
[h] National Centre of Excellence in Geology, University of Peshawar, Peshawar 25130, Pakistan
[i] School of Earth and Space Science, Peking University, Beijing 100871, China
[j] Institute of Geochemistry, Chinese Academy of Sciences, Guiyang 550081, China

ARTICLE INFO

*Article history:*
Received 16 September 2022
Received in revised form 18 November 2022
Accepted 18 November 2022
Available online 25 November 2022

Editor: Dr. Brian Jones

*Keywords:*
Carbonate microfacies
Sequence stratigraphy
Geochemistry
Cambrian strata
North China Platform

ABSTRACT

The Cambrian carbonate sequence in North China is of significant global and regional scientific importance due to its continuous and thick exposure and the data on the major environmental changes and biological events of the early Phanerozoic, which can be gleaned from it. While the well-exposed Cambrian outcrops have been utilized to unravel the processes governing these events, few studies have focused on the outcrops' spatio-temporal depositional patterns and geochemical variations. Therefore, our study address, these issues by integrating fieldwork with petrographic and geochemical analyses. In the North China Platform (NCP), the Cambrian carbonate sequence is predominantly composed of six third-order depositional sequences (~370–400 m thick) that can be divided into nine microfacies, representing three primary microfacies associations, namely tidal flat, lagoon, and shoal. In contrast to the standard carbonate sequence stratigraphy model and many other examples of Cambrian platforms, the deposition of oolitic grainstones in the NCP are overlain by the deep-water calcareous mudstone and shale during a period of slow fall of sea-levels. Such a particular style shows a similar trend to the Schlager model of a type III sequence boundary that formed between a highstand systems tract (HST) and a transgressive system tract (TST). Scanning electron microscope (SEM) observations show an abundance of microbial fossils, a nanosphere, and remnants of extracellular polymeric substances (EPS) inside the dark micrite of normal regressive deposits (oolitic grainstone), suggesting the significant role of microbial activity in the formation of ooids. The $\delta^{18}O$ isotopic values range from −4.15 to −11.75‰ VPDB, portraying pervasive diagenetic alterations with a variable degree of diagenesis at different localities, and both marine- and burial-related diagenesis. In contrast, the $\delta^{13}C$ VPDB values have a very narrow range, from −2 to +2‰ VPDB, suggesting little to no influence of meteoric diagenesis. At the same time, the slight depletion of $\delta^{13}C$ isotope values may reflect the role of microbial processes during the genesis of ooids. This study highlights the importance of microbial activity and marine-related diagenetic overprints during the formation of carbonate facies in the Cambrian Period and provides evidence that carbon isotopic excursions observed during different major environmental and biological events in the NCP are related to primary signals and not altered by intensive meteoric diagenesis.



## 1. Introduction

In carbonate systems, from the Precambrian to the Quaternary, the occurrence of different dominant carbonate factories is significantly influenced by the physical, chemical, and biological evolution of the Earth system (Schlager, 2003; Pomar and Hallock, 2008; Swart, 2015). The

* Corresponding author at: School of Earth and Space Science, Peking University, Beijing 100871, China.
*E-mail address:* tehseenabbas11@yahoo.com (T. Zafar).

https://doi.org/10.1016/j.sedgeo.2022.106301
0037-0738/

transition from the Precambrian to the Cambrian is of great interest because it represents major environmental and biological changes during the "Cambrian Explosion", as recorded in the carbonate rocks (Bottjer et al., 2000; Vickers-Rich and Komarower, 2007; Sperling and Stockey, 2018; Wood et al., 2019; Zhang and Shu, 2021). This transition represents a major evolution of reef-building organisms from Precambrian microbialite-dominated reefs to Phanerozoic metazoan-dominated reefs (Rowland and Shapiro, 2002; Theisen and Sumner, 2016; Chen et al., 2019). Furthermore, Precambrian carbonate platforms consist mainly of reef-like stromatolites, while Cambrian carbonate platforms are largely dominated by mixed burrowed mudstones and ooidal-peloidal grainstone facies (Batten et al., 2004; DiBenedetto and Grotzinger, 2005; Koeshidayatullah et al., 2020).

Cambrian platforms had experienced major depositions of micrite prior to the Ordovician metazoan radiation event (Sepkoski, 1997; Myrow et al., 2004; Pruss et al., 2010). This phenomenon has prompted investigations globally on various aspects of the Cambrian strata, focusing particularly on the dominant carbonate factories and platform morphologies that indicate both ramp-shaped and rimmed-like geomorphologies (rimmed by marginal microbial reefs and ooidal shoals, depending on the architecture of the basin) (e.g., Magaritz et al., 1986; Montanez and Osleger, 1993; Meng et al., 1997; Ivantsov et al., 2005; Collom et al., 2009). In the North China platform (NCP), the Cambrian storm deposits and their stratigraphic attributes have been described by Meng et al. (1986), the sedimentary facies by Feng et al. (1990), the forming mechanism of oolitic limestone in the Zhangxia Formation by Wang et al. (1990), the sequence stratigraphy and depositional trends of the Cambrian-Ordovician strata by Meng et al. (1997), and carbonate microfacies and sedimentary facies by Zhang et al. (2009). However, the majority of these studies have discussed the macro- and microfacies, as well as sequence stratigraphic overviews, of a particular section of the NCP in order to decode and interpret their depositional history (Pan et al., 2019; Xiao et al., 2020a), while the comparative as well as detailed geochemical and isotopic records in various sections of the NCP are still unexplored.

Therefore, the present work aims to provide a framework for a comparative study of the sedimentary facies of the Cambrian strata at several locations in the NCP, namely the Kelan (Shanxi Province), Kouquan (Hebei Province), and Qingshuihe (Inner Mongolia Province) sections. In addition, this study highlights how geochemical signals provide information about the geochemical archive of the Cambrian strata and retrieves the diagenetic environments during deposition of these sediments in the NCP.

## 2. Geological setting

The study area includes the Kelan, Kouquan, and Qingshuihe sections of the NCP, which are situated in Shanxi, Hebei, and Inner Mongolia regions, respectively (Figs. 1 and 2). The NCP is bounded by major suture zones such as the Hinggan Fold Belt to the north, the Qinling Dabieshan Belt to the south, and the Tanlu Fault to the east (Meng et al., 1997) (Fig. 1b). The NCP began to subside during the late Neoproterozoic (Wang et al., 2000) and received clastic input during flooding of the Qin Ling Sea, located to the south-southeast, in the middle Terreneuvian that prevailed at its eastern, western, and southern margins (Meng et al., 1997). A great unconformity (Precambrian-Cambrian contact) was produced by geological processes, and possibly triggered the Cambrian explosion, a case very similar to North America and other places (Peters and Gaines, 2012). The mixed succession of siliciclastic and carbonate sediments (~1800 m thick) was deposited on the NCP during Cambrian Series 2 and into the Late Ordovician (Meyerhoff et al., 1991). After a platform-wide hiatus in the middle Paleozoic (Late Ordovician to Early Carboniferous), coal-bearing, shallow marine and continental deposits accumulated on the platform during the Carboniferous and the Permian (Lv and Chen, 2014). Deposition on the platform was terminated in the Early Triassic by regional uplift that resulted from the collision between the North China Block and the South China Block (Lee and Chough, 2006). An approximately 700 m thick Cambrian succession was deposited on the NCP (Fig. 3). Terreneuvian and early Series 2 records are absent in most parts of the NCP. The rest of the Cambrian record can be approximately subdivided into three successions in ascending order (Ma et al., 2017; Latif et al., 2018; Riaz et al., 2019a, 2019b): 1) most of the mixed succession of Series 2 and early Miaolingian, composed of red beds and carbonate rocks; 2) carbonate strata of the middle to late Miaolingian dominated by oolitic grainstones; 3) carbonate succession of the Furongian, composed mainly of carbonate muds and shallow ramp limestone. Based on this thick depositional succession revealed by cyclic sedimentation (Mei et al., 2005; Mei, 2011; Latif et al., 2018; Riaz et al., 2019a, 2019b, 2022a), a new scheme of lithostratigraphic division has been proposed from the lithostratigraphic scheme of Meng et al. (1997) and been discussed in terms of a broad chronostratigraphic division (see Peng et al., 2012; Peng and Zhao, 2018). According to this scheme, the Cambrian strata can be divided into nine third-order sequences: the Dalinzi, Jianchang, Mantou, Maozhuang, Xuzhuang, Zhangxia, Gushan, Changshan, and Fengshan formations (Mei, 2011) (Fig. 3).

The Cambrian strata in the studied sections of the NCP have nonconformable lower and unconformable upper contacts with Precambrian and Ordovician strata, respectively. In the Kelan section, the Huoshan Formation nonconformably overlies the Mesoproterozoic Wumishan Formation. It was deposited during early transgression and forms the first third-order depositional sequence ($DS_1$) (Riaz et al., 2019a). In the Kouquan and Qingshuihe sections, the Xuzhuang Formation presents a nonconformity with overlies Archean metamorphic rocks. In all the studied sections, a disconformity developed between the Furongian Fengshan Formation and the Ordovician Yeli Formation.

## 3. Materials and methods

The studied Kelan (~374 m), Kouquan (~372 m), and Qingshuihe (~397 m) sections are exposed in the Shanxi, Hebei, and Inner Mongolia regions of the NCP respectively (Figs. 2, 4). The Kelan section (38° 44′ 41″ N, 111° 34′ 45″ E) comprises the northwestern part of the Shanxi province in Luya Mountain (Figs. 1c; 2a–f). The Kouquan section (39° 46′ 14.2″ N, 114° 51′ 30.6″ E) is 30 km southeast of Yuxian city in Hebei province along the road from Kouquan town to Muxu town (Figs. 1d; 2a–f). The Qingshuihe section (39° 54′ 27.2″ N, 111° 39′ 59.1″E) is 3 km east of Qingshuihe town and forms the western boundary of the platform (Figs. 1e; 2a–f). The Fengshan Formation is not exposed in the Qingshuihe section, but can be observed in cuts along the G-109 Highway which runs to Ordos city in Inner Mongolia.

During the field work, the Cambrian strata of the Miaolingian (Xuzhuang, Zhangxia, Gushan formations) to Furongian (Changshan and Fengshan formations) age of the Kouquan and Qingshuihe sections were subdivided into six third-order level depositional sequences, while the Kelan section was subdivided into seven (Fig. 4). The division of the Cambrian strata in studied sections are similar to the other sections of the NCP as described by Mei et al. (1997), Mei (2011), Latif et al. (2019), and Riaz et al. (2019a, 2019b). Moreover, several other field observations of lithofacies, sedimentary structures, and meter-scale sedimentary cycles were also studied during the field work. A detailed lithological log of the field studies of carbonate facies has been prepared (see Fig. 4).

Petrographic analysis of 236 randomly collected samples across the Miaolingian and Furongian intervals was carried out (Fig. 4). To determine the sedimentary fabrics, thin sections were studied under the Zeiss Axio Scope A1 microscope at the China University of Geosciences, Beijing. Geochemical analyses were carried out to understand the microbial contribution during the formation of carbonate facies. Scanning Electron Microscopy (SEM; JEOL, JSM-7800F) investigations of the carbonate facies were conducted on thin etched sections. Some of these

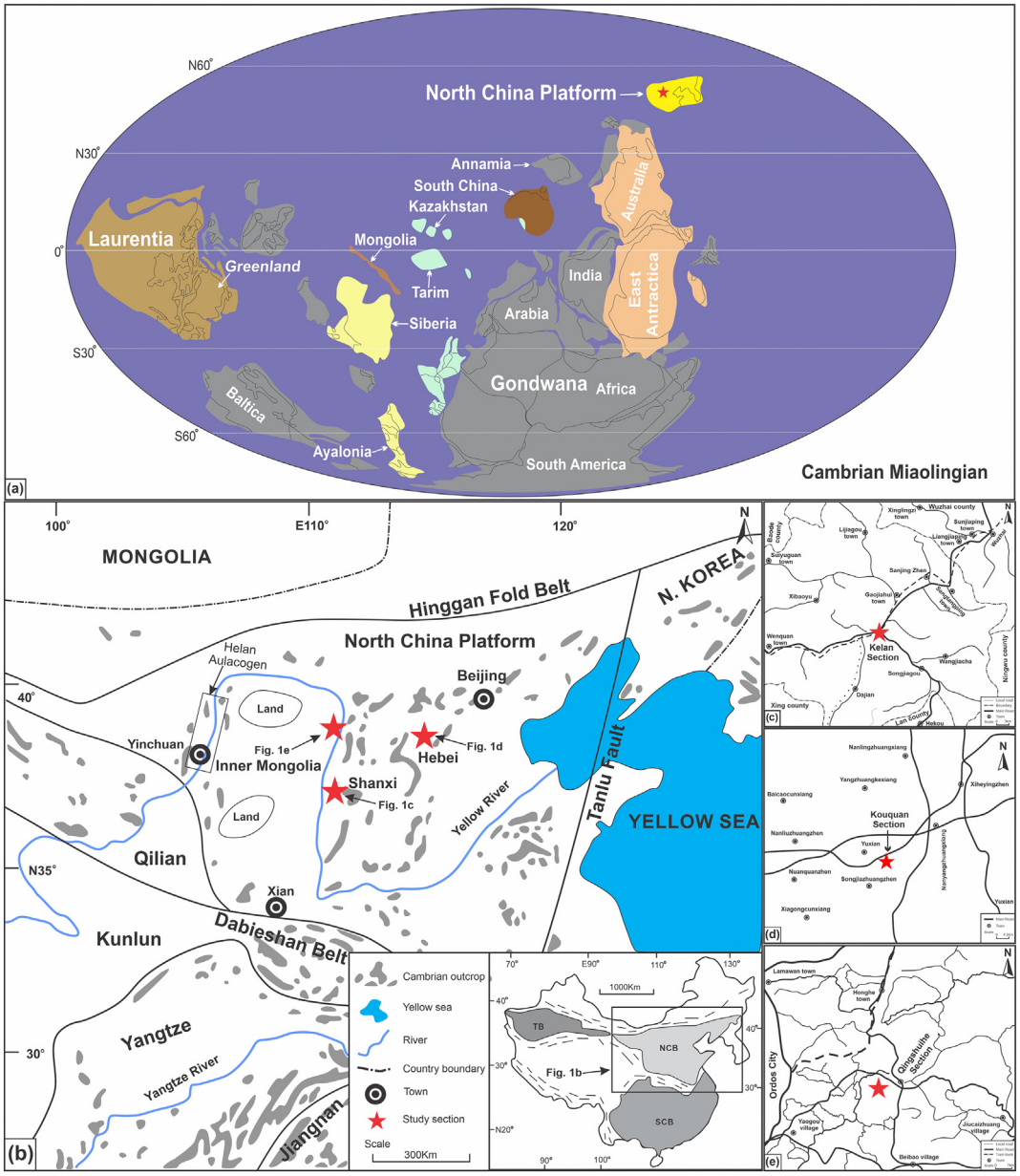


**Fig. 1.** (a) Global position of the NCP in the Miaolingian (modified after Riaz et al., 2020); (b) NCP and associated blocks, showing the study area by red stars (modified after Myrow et al., 2015; Riaz et al., 2019a, 2019b); (c, d, e) Show location maps of Kelan, Kouquan and Qingshuihe sections in the Shanxi, Hebei, and Inner Mongolia Provinces, respectively.

samples were gold coated, depending on whether they were prepared for textural observation or micro analysis. Semi-quantitative elemental investigation of spots was achieved by Energy Dispersive X-ray (EDX; TEAM Apollo XL) spectroscopy. High voltage (10.0 Kv) and pulses (5.45–51.82 kcps) were used. In addition, fluorescence microscopic study was employed to examine the interior of the carbonates, whereas Electron Probe Micro Analysis (EPMA; EPMA-1600) was used to investigate mineral chemistry. The EPMA-based elemental study of CaO, MgO, $Na_2O$, $K_2O$, $Al_2O_3$, and $SO_3$ was conducted under working conditions of 15-kV accelerating voltage, 20 nA beam current, and 10 s counting time. Additionally, $\delta^{13}C$ and $\delta^{18}O$ isotopic analyses were performed on 81 samples taken from the bottom to the top of the Cambrian sequence of three studied sections. Micro-samples were prepared by micro-drilling fresh rock surfaces (in the case of micritic samples) and were sometimes carefully taken under the microscope from ooid accumulations in thin sections (in the case of grainstone samples). These samples were measured using a dual-inlet VG SIRA 10 (VG Iso-Gas Limited, Middlewich, Cheshire, UK) mass spectrometer in the Chinese Academy of Sciences, Beijing by reacting 4 to 5 mg of powdered sample material with anhydrous phosphoric acid at 50 °C (ca. 48 h) for carbonate samples, and reported based on Vienna Pee Dee Belemnite (VPDB). Moreover, the precision of the $\delta^{13}C$ and $\delta^{18}O$ isotopic ratios for duplicate analyses was better than ±0.1‰.

## 4. Results

### 4.1. Sedimentary characterization

The Miaolingian record in the studied sections of the NCP comprises the Xuzhuang, Zhangxia, and Gushan formations (Figs. 4, 5a). The Cambrian Xuzhuang Formation can be subdivided into three parts: (i) lower red beds, comprising fine clastic sedimentary strata; (ii) middle calcareous shale; and (iii) upper oolitic limestone (Figs. 5b, 6a, b). The cross-laminations were also observed in oolitic limestone at the Kelan section

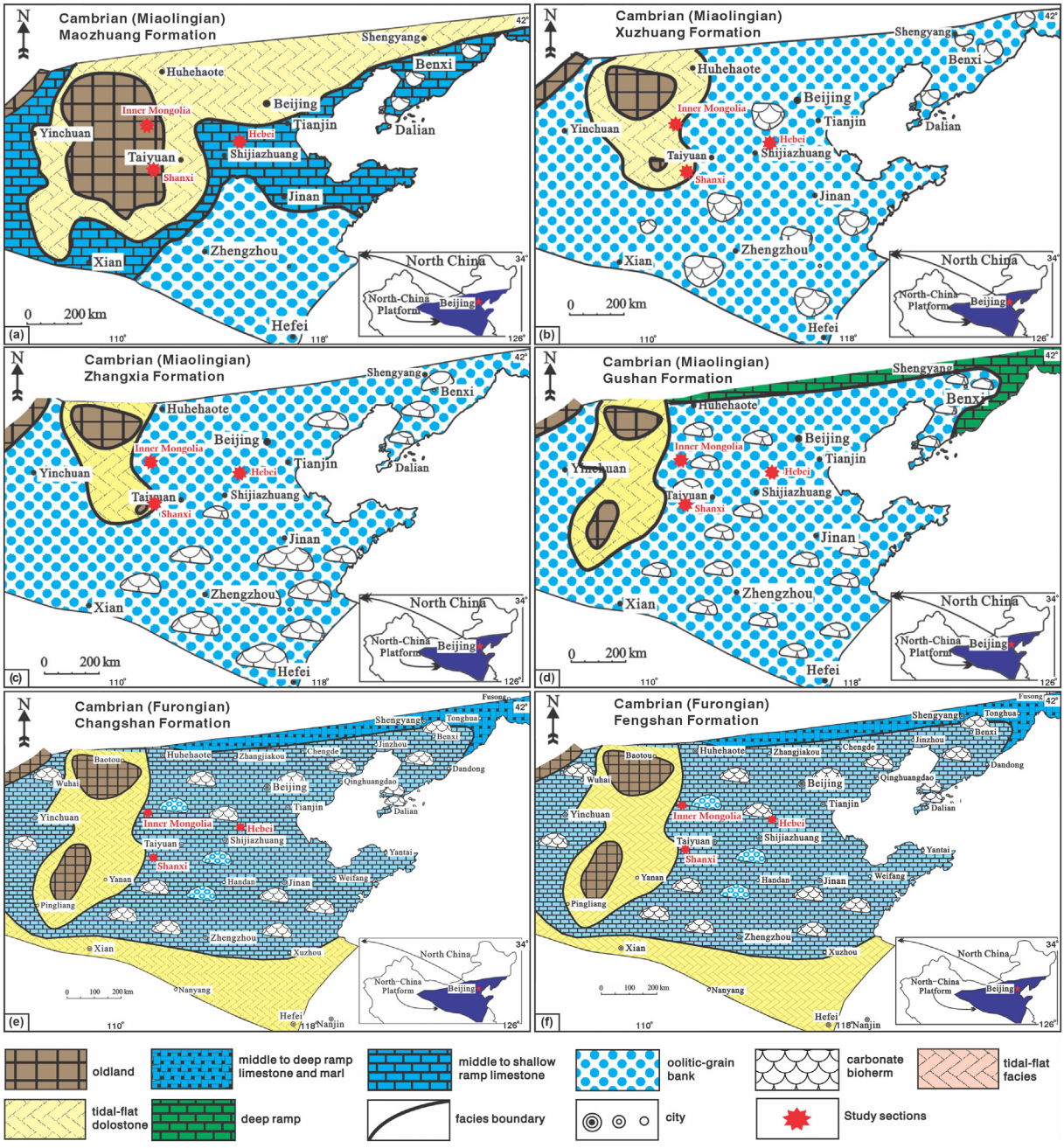


**Fig. 2.** (a–f) Paleogeographical setting of the Cambrian (Miaolingian-Furongian) strata of the North China Platform (Adapted from Feng et al., 1990, 2004). The red stars show the studied sections of the NCP.

(Fig. 7a). The Zhangxia Formation can be subdivided into three subsequences, as identified according to the composition and cyclicity of sedimentary facies (Figs. 4, 5a, c). In each subsequence, calcareous mudstone is overlain by banded micrite and oolitic limestone (Figs. 4, 6c). The oolitic limestone at the Qingshuihe section contains evidence of burrowing, scoured surfaces and spar-filled calcite veins (Fig. 7b). The upper contact of the Zhangxia Formation, which is possible hardground, makes conformable upper contact with the interbedded micritic limestone and marl of the Gushan Formation (Fig. 7c), and the lower contact is with the Xuzhuang Formation (Figs. 5a, c, 6a), in all studied sections of the NCP (Fig. 4). The lower part of the Gushan Formation contains calcirudite within interbedded micritic limestone and marl (Fig. 6d, e). The middle part of the formation comprises micritic limestone interbedded with calcareous mudstone, whereas the upper part of the formation consists of interbedded thin micritic limestone and thick oolitic limestone (Figs. 4, 5d, 6f). The scoured surfaces occur in the oolitic limestone at the Kouquan and Qingshuihe sections (Fig. 7d, e), whereas desiccation cracks were identified in micritic limestone from the upper part of the formation at the Qingshuihe section (Fig. 7f). The Gushan Formation makes conformable upper contact with the calcareous mudstone and shale of the Changshan Formation of the Furongian series (Figs. 5d, 7g).

The Furongian record at all studied sections consists of the Changshan and Fengshan Formations (Figs. 4, 5e, f). The condensed section in the lower part of the Changshan Formation is comprised of calcareous mudstone and shale (Fig. 5d), which is overlain by the massive calcareous mudstone and banded micrites, which comprise the middle part of the formation (Fig. 4). At the Kouquan section, mud cracks were observed in calcareous mudstone (Fig. 7h). The upper Changshan Formation consists of interbedded thin micritic limestone

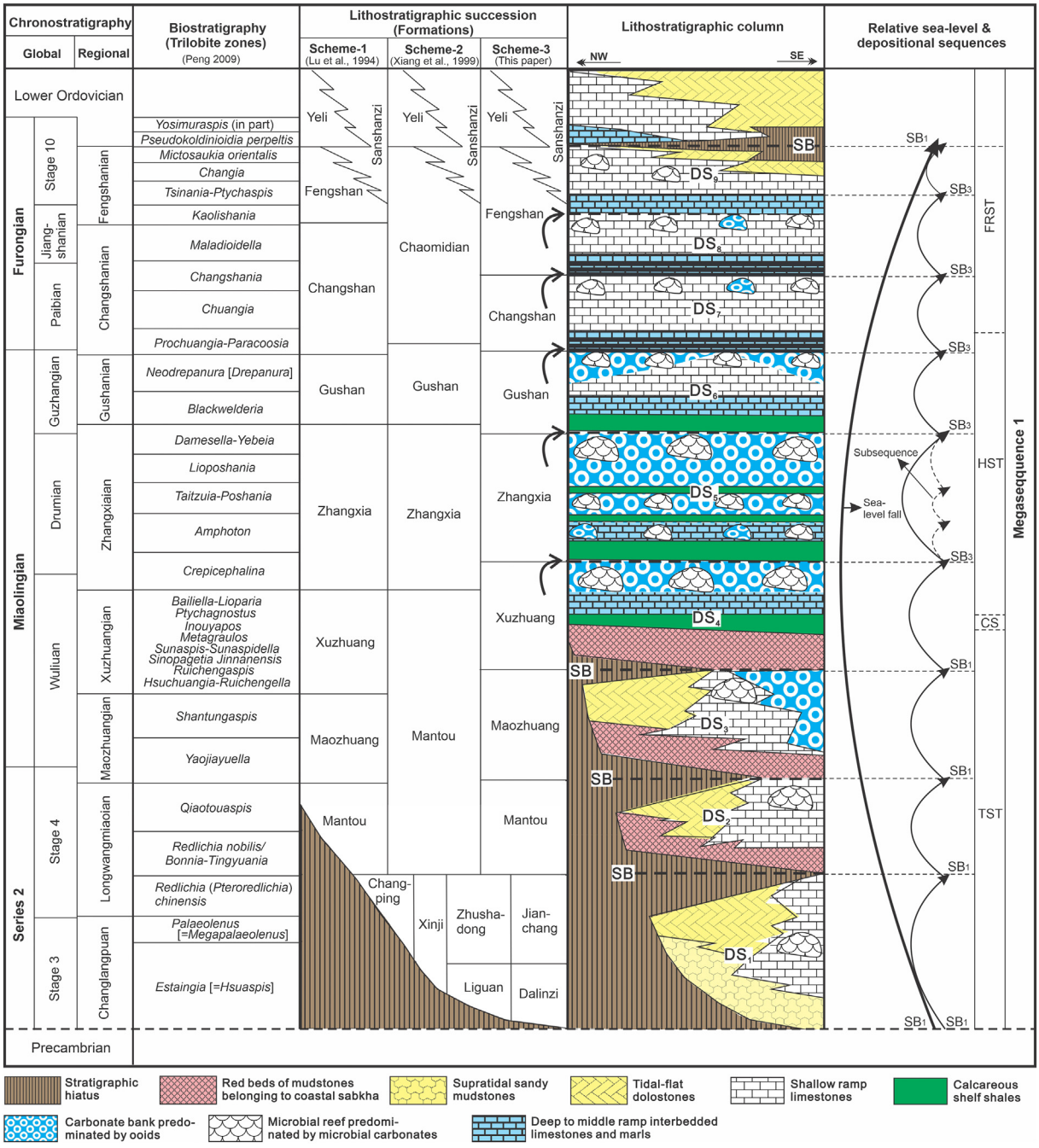


**Fig. 3.** Integrated stratigraphy showing the sedimentary succession of nine third-order sequences ($DS_1$ to $DS_9$) of the Cambrian in NCP along with two types of sequence boundaries i.e., exposure surface and drowning unconformity surface (arrows) (modified after Mei et al., 2020a, 2021). Trilobite zones (Peng, 2009), Lithostratihraphic succession (Scheme-1: Lu et al., 1994; Scheme-2: Xiang et al., 1999). Abbreviations: DS: Third-order depositional sequence; SB: Sequence boundary.

and thick oolitic limestone (Fig. 4). The oolitic limestone was observed in the upper part of the Changshan Formation at the Kelan section (Fig. 6g), whereas the same stratigraphic interval at the Kouquan and Qingshuihe sections grades into fossiliferous limestone with few beds of ooids and bioherms (Figs. 4, 5e, 6h). The fossiliferous limestone at the Qingshuihe sections contains evidence of boring/burrowing (Fig. 7i, j). The lower and upper boundaries of the Changshan Formation show a rapid transition, which developed during a rapid sea-level rise (Figs. 4, 5d, e, 7k). The Fengshan Formation at the Kelan section is composed of two depositional sequences (Fig. 4). The first depositional sequence consists of calcareous mudstone and shale in the lower part, calcareous mudstone interbedded with micritic limestone in the middle part, and oolitic limestone interbedded with thin micritic limestone in the upper part of the formation (Fig. 6i), distinguishing it from other studied sections that consist of fossiliferous limestone (Fig. 4) in the upper part of the formation. L-M (limestone-marl) type cycles were found in the lower part of the first depositional sequence at the Kelan section, whereas subtidal type cycles were observed in middle to upper parts (Fig. 7l, m). The upper and lower boundaries of the first depositional sequence are conformable (Fig. 5e-f). The second depositional sequence consists of calcareous mudstone interbedded with banded micritic limestone in the lower part of the formation with thin beds of micrite and massive fossiliferous limestone in the middle part (Figs. 4, 5f, 6j). The overlying upper part consists of medium bedded dolomitic limestone merging into massive muddy dolomite (Fig. 4). The lower and upper boundaries of the second depositional sequence contact the first depositional sequence of the Fengshan Formation and the lower Ordovician Yeli Formation, respectively.

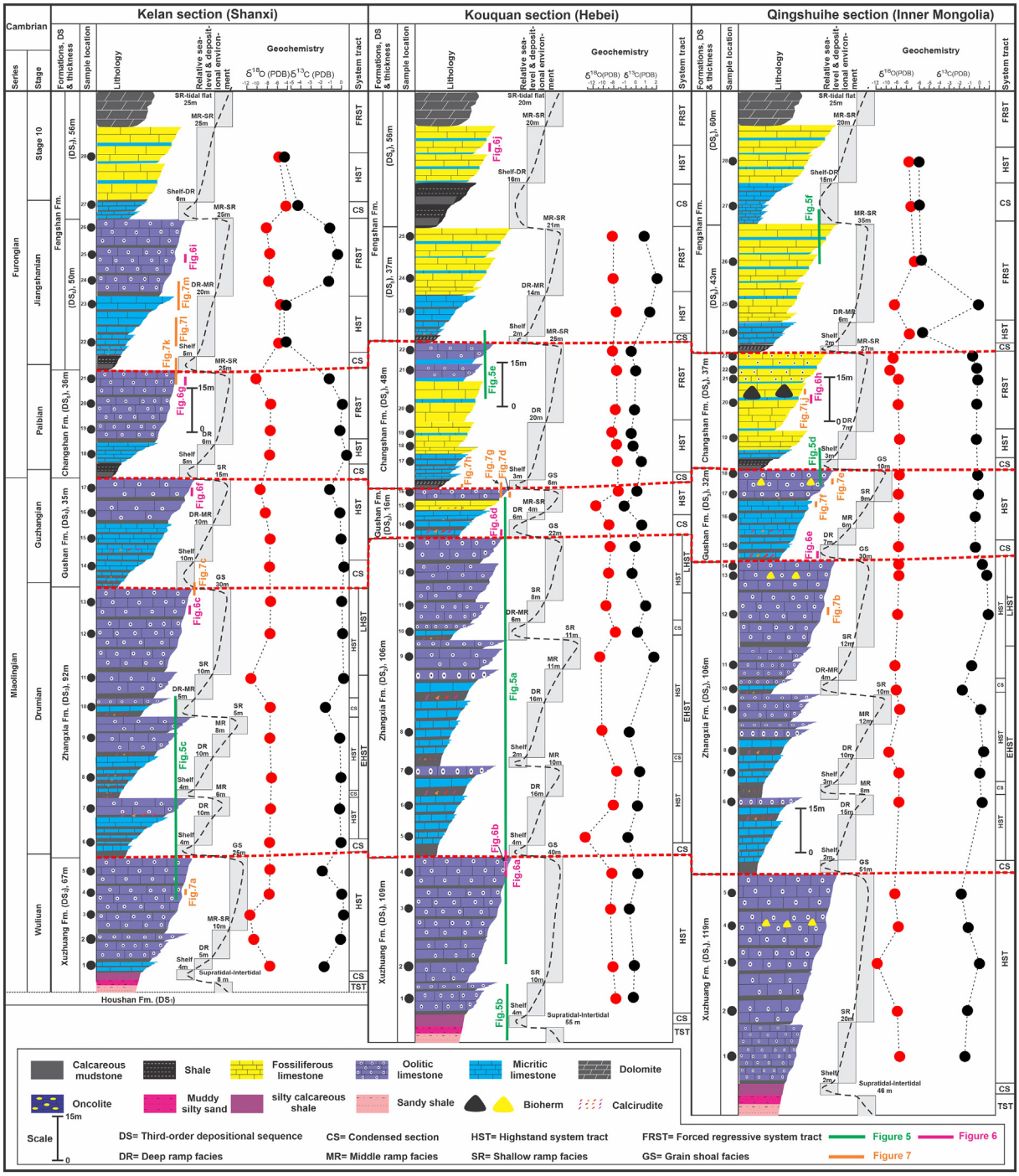


**Fig. 4.** Integrated Cambrian stratigraphic charts of Kelan, Kouquan, and Qingshuihe sections. Carbon and oxygen isotopic records are also plotted.

The Xuzhuang Formation at all three studied sections contains red beds in the lower part, calcareous mudstone in the middle part, and thick bedded oolitic grainstone interbedded with thin micritic limestone in the upper part, reflecting the relative rise and slow fall of sea levels (Figs. 5b, 6a, b). The red beds indicate the supratidal setting (Mei et al., 1997; Meng et al., 1997) and the calcareous mudstone represents the condensed interval deposited during the shelfal to deep ramp settings (Riaz et al., 2019a, 2019b), whereas the oolitic limestone interbedded with thin micritic limestone as well as cross-laminations suggests a shallow but high-energy setting (Riaz et al., 2022a).

The Zhangxia Formation exhibits three subsequences similar to the other records of the NCP (see Latif et al., 2018; Riaz et al., 2019a, 2019b), which can be distinguished based on flooding surfaces (Figs. 4, 5a, c). Each subsequence of the Zhangxia Formation shows shelfal to deep ramp settings (calcareous mudstone) that represent the condensed intervals of each sequence and middle to shallow ramp settings (thick oolitic limestone interbedded with thin micritic limestone) (Riaz et al., 2019a). Further signs of burrowing, scoured surfaces and spar-filled calcite veins in the upper part of the oolitic limestone potentially provide evidence for hardground (Fig. 7b).

The Gushan Formation contains calcirudites within micritic limestone and marl that depict depositional conditions different from those of the Xuzhuang and Zhangxia formations (Meng et al., 1997). Calcirudites indicate that severe transgression started from the Gushan Formation, as compared to the early and middle Miaolingian record (the Maozhuang, Xuzhuang, and Zhangxia Formations) (see Mei, 2011). The

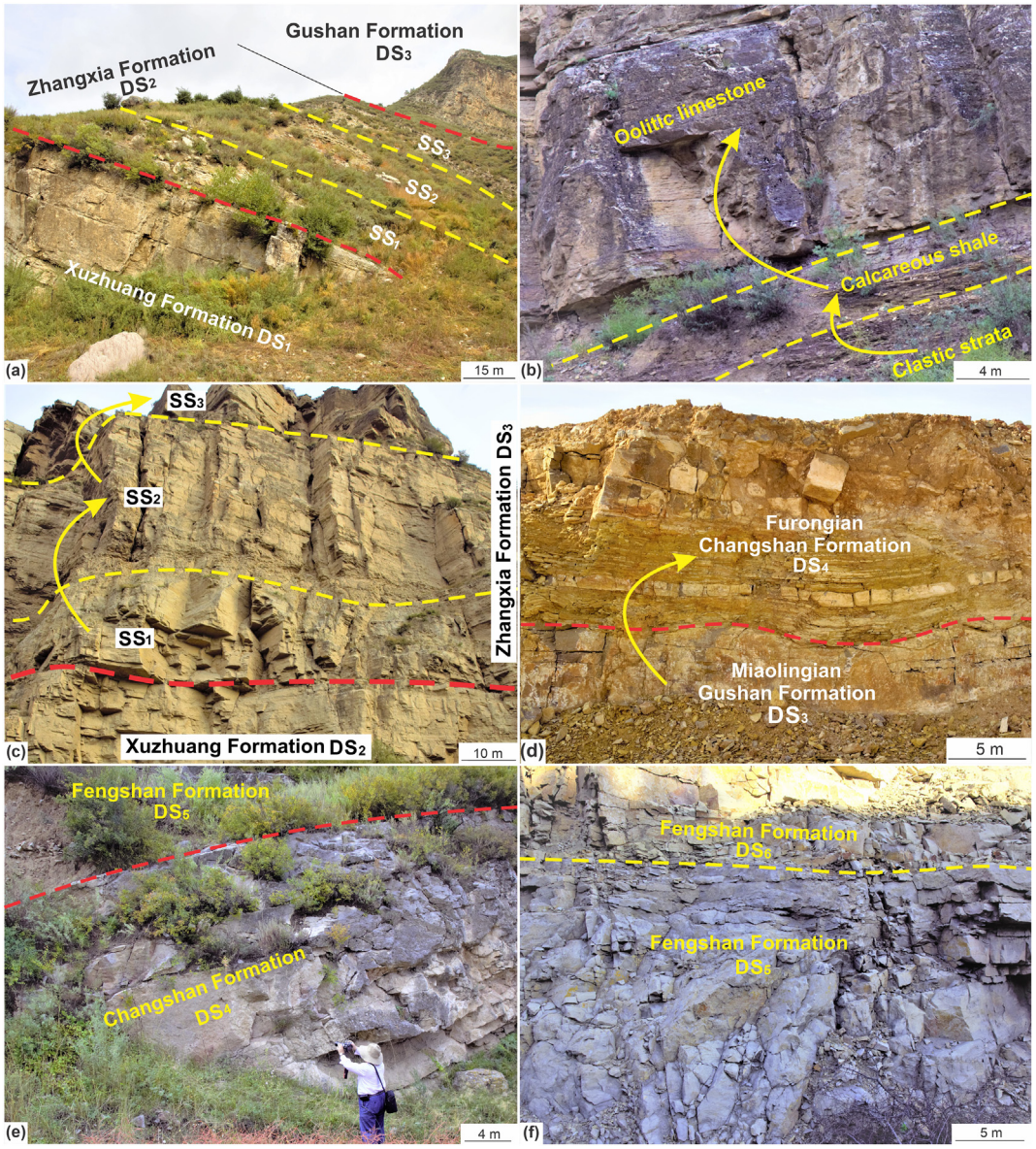


**Fig. 5.** The sedimentary fabric of the Cambrian record at Kelan, Kouquan, and Qingshuihe sections of the NCP. (a) Conformable contact of Miaolingian strata among Xuzhuang Formation ($DS_1$), three subsequences of the Zhangxia Formation ($DS_2$), and Gushan Formation ($DS_3$) at Kouquan section; (b) Xuzhuang Formation comprises beds of red clastic strata in the lower, calcareous mudstone in the middle, and oolitic limestone in the upper part of the formation at Kouquan section. Condensed section (calcareous mudstone) separated the *platform initiation* stage from *platform foundation stage*; (c) Three subsequences of the Zhangxia Formation ($DS_3$) at Kelan section. The Zhangxia Formation shows conformable lower contact with the Xuzhuang Formation; (d) Contact between oolitic limestone of the Gushan Fm. and interbedded calcareous mudstone and shale of the Changshan Fm. indicates drowning unconformity at the Qingshuihe section; (e) The boundary between the Changshan ($DS_4$) and Fengshan formations ($DS_5$) at Kouquan section. The boundary separates the fossiliferous limestone with few beds of ooids of the upper part of the Changshan Formation, and calcareous mudstone and shale of the lower part of the Fengshan Formation; (f) Two depositional sequences ($DS_5$-$DS_6$) of the Fengshan Formation are exposed beside the G109 road to the Ordos city. Abbreviations: DS: Third-order depositional sequence; SS: Subsequences.

oolitic limestone, as well as the scoured surfaces in the upper part of the Gushan Formation, provide evidence for a high-energy shallow ramp setting (Fig. 7d, e). Furthermore, desiccation cracks in micritic limestone also provide evidence of subaerial exposure (Fig. 7f).

The lower part of the Furongian Changshan Formation comprises calcirudite, similar to the lower part of the Gushan Formation, indicating a severe transgressive event during the Furongian. The upper part of the Changshan Formation contains oolitic limestone and in some sections shows boring and burrowing in fossiliferous limestone (Fig. 7i, j); together, these observations provide evidence of deposition along a shallow ramp setting (Riaz et al., 2022a). The upper boundary of the Changshan Formation provides a typical example of drowning unconformity (Fig. 7k) similar to the upper boundary of the Gushan Formation (Fig. 7g).

The first third-order sequence of the Fengshan Formation indicate shelf to deep ramp settings (calcareous mudstone) (Figs. 4, 5e) and middle to shallow ramp settings (micritic limestone and oolitic limestone) (Fig. 4, 5f), reflecting the rise and fall of sea levels (Riaz et al., 2019a, 2019b). Additionally, the deep to middle-ramp calcareous mudstone interbedded micritic limestone, and the shallow-ramp oolitic limestone at Kelan section cover many meter-scale cycles (e.g., Mei, 1993; Mei et al., 2000, 2005) that frequently form a regularly vertical stacking pattern in the third-order sequence (Fig. 7l, m). This series of deposits provides a typical example for the study of sequence stratigraphy from cycles to sequences, from litho- to sedimentary-facies successions, and from changes of water-depth to variations in relative sea level (Fig. 7l, m) (see Mei et al., 2005; Riaz et al., 2022a). The lower part of the second third-order sequence shows a similar depositional trend to the first third-order

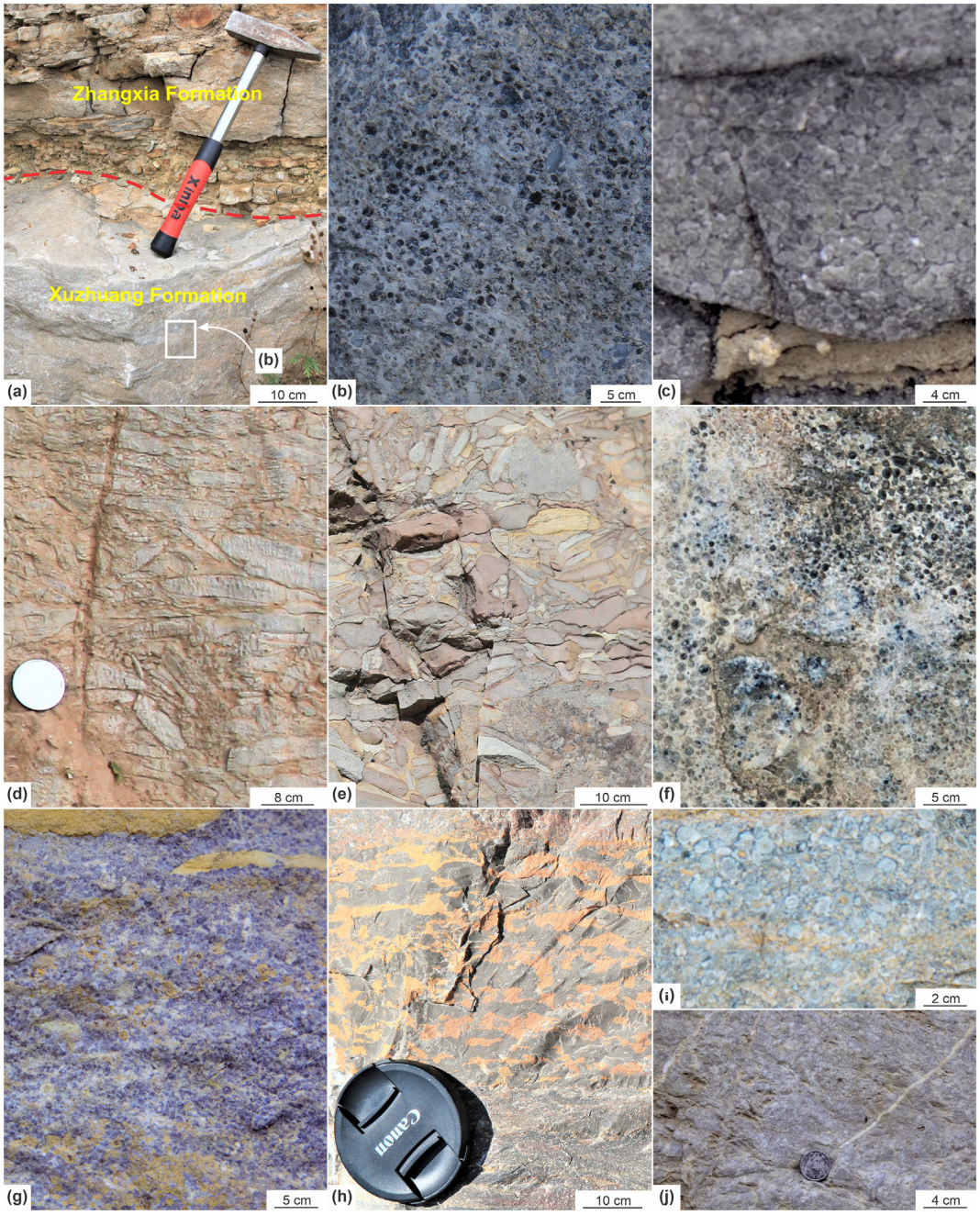


**Fig. 6.** Mesoscale features of the Cambrian record at the studied sections of the NCP. (a) Contact between Xuzhuang Formation and Zhangxia Formation at Kouquan section; (b) Oolitic grainstone in the upper part of the Xuzhuang Formation at Kouquan section; (c) Oolitic grainstone in the Zhangxia Formation at Kelan section; (d, e) Calcirudites in the lower part of the Gushan Formation at Kouquan section and Qingshuihe section, respectively; (f) Oolitic limestone in the upper part of the Gushan Formation at Kelan section; (g) Oolitic limestone in Changshan Formation at Kelan section; (h) Micritic and fossiliferous limestone in the Changshan Formation at Qingshuihe section; (i) Oolitic limestone in first third-order sequence of the Fengshan Formation at Kelan section; (j) Fossiliferous limestone in second third sequence of the Fengshan Formation at Kouquan section.

sequence, but the upper part is replaced by medium bedded dolomitic micrite, suggesting shallow ramp to tidal flat settings (Mei et al., 2005). The contacts between the massive oolitic limestone of the Xuzhuang, Zhangxia, and Gushan formations (Figs. 4, 5b, 6b, c, f) and the calcareous mudstone of the Zhangxia, Gushan, and Changshan formations (Figs. 4, 5d, 7g, k, c) exhibit the rapid transition in the studied sections, similar to the drowned unconformity of type III described by Schlager (1989, 1999).

### 4.2. Microfacies: identification and interpretation

Three major microfacies (MF) associations (flat, lagoon, and shoal facies) and nine subdivisions have been identified along the studied sections. A detailed description of these microfacies (landward to basinward) is provided below.

MF1: Mudstone and microbial mudstone microfacies (MF1) can be observed at all sections. MF1 can occasionally be seen as microbial mudstone and micritic limestone (Fig. 8a-e). Under the microscope, mudstones are characterized by a scarcity of allochems and sedimentary structures (Fig. 8a). Microbial mudstone facies are composed of dark and dense patches of micrite (Fig. 8b–e). High-resolution imaging shows that the micrite patches consist of tubular structures (Fig. 8c, e) and bulbous structures (Fig. 8d inset image).

The tubular structures in dark patches of micrite (Fig. 8c, e) are possibly composed of the calcified sheaths of filamentous fossils of

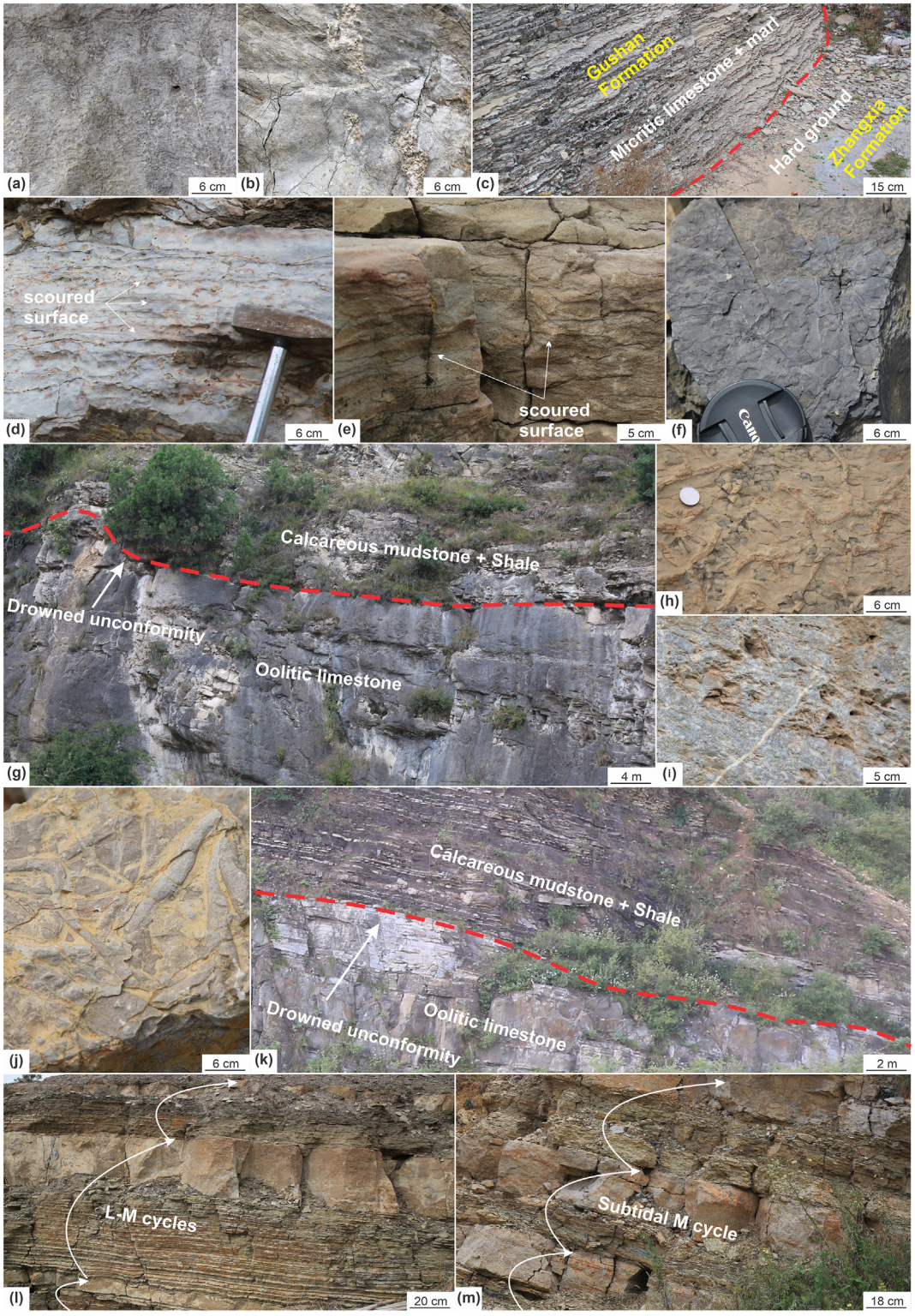


**Fig. 7.** Sedimentary characteristics and depositional style of the Cambrian strata of the NCP. (a) Cross lamination in the oolitic limestone of the Xuzhuang Formation at Kelan section; (b) Burrowing, scoured surface and spar filled calcite vein in the oolitic limestone of the Zhangxia Formation that provide a typical example of hardground in Qingshuihe section; (c) Hardground in the Zhangxia Formation at Kelan section that shows the exposed surface which was covered by deep water interbedded micritic limestone and marl; (d) Scoured surface in the oolitic limestone of Gushan Formation that show their deposition in shallow high energy setting in Kouquan section; (e) Scoured surface in the oolitic limestone of the Gushan Formation in the Qingshuihe section; (f) Desiccation crack (micritic limestone) in the Gushan Formation at Qingshuihe section; (g) An example of drowning unconformity marked with a red dashed line in the Gushan Formation at Kouquan section. Here, Gushan Formation represents oolitic limestone overlies calcareous mudstone and shale of the Changshan Formation; (h) Mud crack in calcareous mudstone of the Changshan Formation at Kouquan section; (i) Boring in the limestone of the Changshan Formation at Qingshuihe section; (j) Burrow in the limestone (i.e., fossiliferous limestone) of the Changshan Formation at Qingshuihe section; (k) A typical example of drowned unconformity in the Changshan Formation at Kelan section of the NCP; (l) L-M cycles developed in lower to middle part of the first depositional sequence of the Fengshan Formation at Kelan section; (m) Subtidal meter scale cycles developed in middle to upper part of the first depositional sequence of the Fengshan Formation at Kelan section.

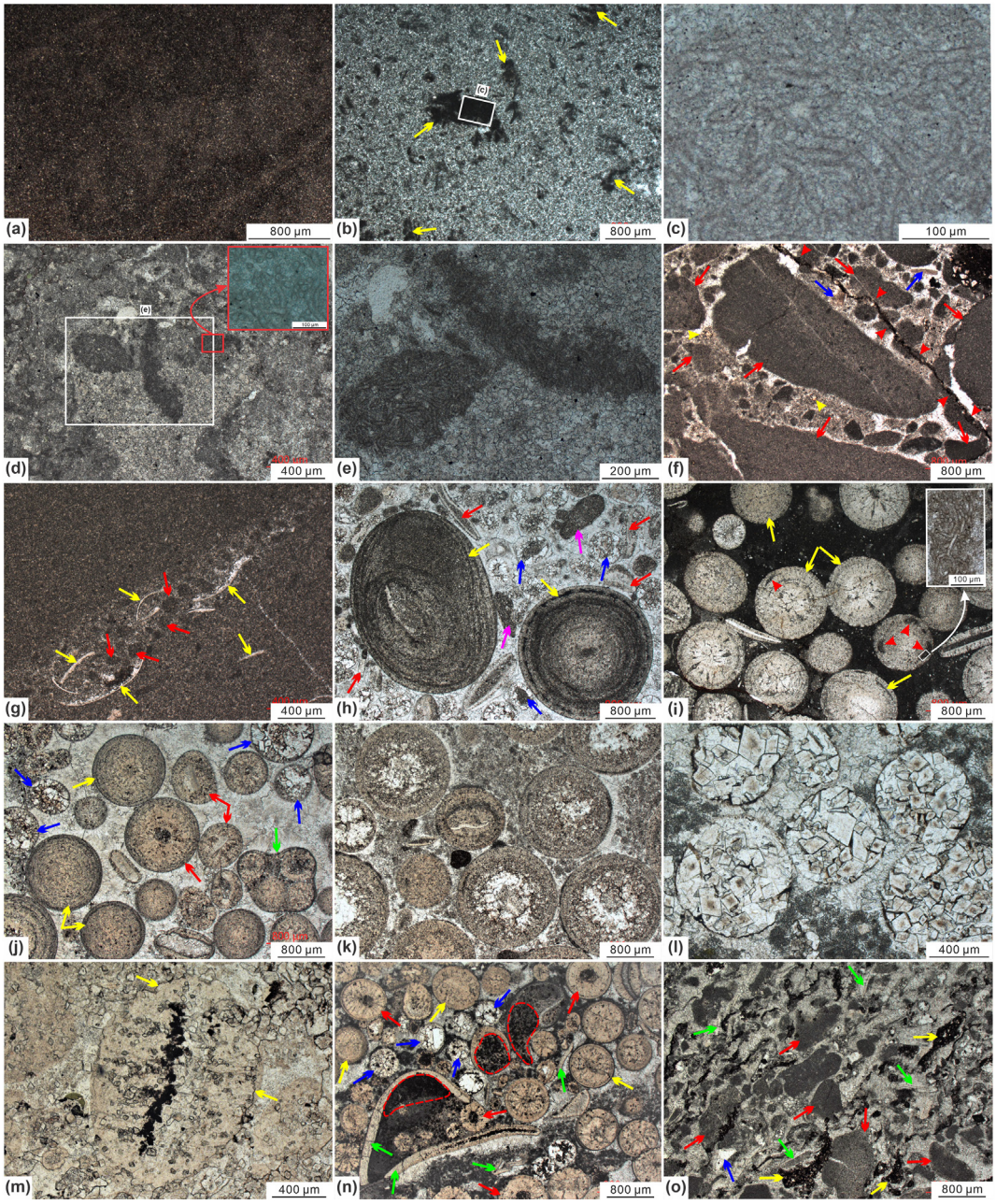


**Fig. 8.** Photomicrographs of microfacies of Kelan, Kouquan, and Qingshuihe sections: (a) MF1 mudstone (the Gushan Formation at Qingshuihe section); (b) MF1 microbial mudstone (the Fengshan Formation at Kelan section) comprises dark patches of micrite (yellow arrow); (c) Zoom of figure b shows tubular structure of the abundance of filamentous (*Girvanella*-type) cyanobacteria within the dark micrite; (d) MF1 microbial mudstone contains dark and dense patches of micrite. The inset image shows the bulbous structure of the sulfate-reducing bacteria; (e) Zoom part of rectangle in figure d shows a cluster of filamentous (*Girvanella*-type) cyanobacteria; (f) MF2 (the Fengshan Formation at Kouquan section) is usually composed of brachiopod debris (blue arrows), variable sized intraclasts (red arrows), quartz grains (yellow arrow heads), and fractures (red arrow heads); (g) MF3 (the Fengshan Formation at Kouquan section) shows trilobite and brachiopod fossil fragments (yellow arrows) and peloids (red arrows); (h) MF4 in Furongian strata mainly includes oncoids (yellow arrows), brachiopod and trilobite remains (red arrows), intraclasts (pink arrows), and neomorphosed ooids (blue arrows); (i) MF5 (Zhangxia Formation at Kelan section) comprises radial-concentric ooids with nuclei of bacterial biofilm (yellow arrows). The cortices of several ooids contain dark and dense micrite (red arrow heads). The zoom part shows the filamentous (*Girvanella*-type) cyanobacteria within the dark micrite; (j) MF6 (Xuzhuang Formation at Qingshuihe section). Microfacies shows the radial-concentric ooids without nucleus (yellow arrows), radial-concentric ooids with nucleus of pellets and broken pieces of brachiopods (red arrows), composite ooids (green arrow), and neomorphosed ooids (blue arrows); (k) MF7 (Zhangxia Formation at Kouquan section) shows the partial dolomitization; (l) MF7 ooidal dolograinstone shows the complete dolomitization in the Fengshan Formation at Kelan section; (m) MF7 (Gushan Formation at Qingshuihe section) shows the tiny crystals of dolomite and pyrite minerals on the center and cortex of ooids. The yellow arrow show the stylolite; (n) MF8 (Changshan Formation at Kouquan section) comprises radial-concentric ooids without nucleus (yellow arrows), radial-concentric ooids with nucleus (red arrows), neomorphosed ooids (blue arrows), brachiopod fossils (green arrows), and probably accumulations of pyrite grains (red dashed lines); (o) MF9 (Changshan Formation at Qingshuihe section) depicts the bioclasts (green arrows), intraclasts (red arrows), scattered dolomite grains (yellow arrows), and quartz grains (blue arrows).

cyanobacteria (*Girvanella* type) (Riding, 2011; Riaz et al., 2020), whereas the bulbous structures (Fig. 8d) indicate sulfate-reducing bacteria (Riaz et al., 2022b). These microorganisms, particularly cyanobacteria, are the major participants in the formation of EPS during photosynthesis and cause the formation of carbonate grains (Latif et al., 2019; Mei et al., 2020a, 2020b, 2021). The noteworthy amount of micrite can be interpreted as sediment deposited in a fairly low-energy setting, with little or no winnowing of the fine mud (Flügel, 2010). Moreover, mudstones barren of fossils represents peritidal carbonates (e.g., Beigi et al., 2017; Jafarian et al., 2017). This microfacies

is best interpreted as representing the upper tidal flat of a supratidal environment.

MF2: Intraclast-bioclast wackestone and packstone microfacies (MF2) (Fig. 8f) can be observed in the Fengshan Formation at the Kouquan section and in the Changshan Formation at the Qingshuihe section. The intraclasts are the main components of this microfacies and may comprise up to 45% of the limestone, while the bioclasts are subordinate and mostly represented by brachiopod and trilobite debris (15% of total volume). The intraclasts range from 0.5 to 2 mm in size and are dark black in colour (Fig. 8f). Moreover, a few quartz grains and fractures were also observed (Fig. 8f).

The dark black intraclasts (Fig. 8f) are reworked carbonates (Flügel, 2010) composed of micrite and represent the exposure of the NCP to severe storm conditions (Flügel, 2010) during the Cambrian (Meng et al., 1997). Additionally, fractures (Fig. 8f) may have originated during the storm itself. The presence of quartz grains reflects the input of terrigenous material. This microfacies shows multi-stage deposition. The environment is inferred to have been predominantly low energy necessary for the micrite deposition, but affected by high energy reworking from time to time. The intraclasts may have originated from nearby tidal flats and been transported into adjacent subtidal settings during major storms.

MF3: Peloid bioclast wackestone (MF3) is present in all three sections. In the Kelan section, it is observed in the Xuzhuang and Zhangxia formations. In the Kouquan section, the microfacies is present in the Gushan and Fengshan formations, whereas at the Qingshuihe section, it is only observed within the Zhangxia Formation (Fig. 8g). MF3 mainly contains bioclast fragments, especially trilobite sclerites (5–15%) and peloids (10–20%) (Fig. 8g).

Most polymerid Cambrian trilobites (Fig. 8g) are indicators of shallow shelf settings and are the main textural components in rocks of Cambrian-Ordovician age (Scholle and Ulmer-Scholle, 2003). The presence of micrite, peloids, and the lack of marine cement in this microfacies points to deposition in relatively low-energy conditions such as lagoonal environments (Amel et al., 2015).

MF4: Ooid intraclast oncoid bioclast packstone and grainstone (MF4) were observed in all studied sections. The bioclast fragments are primarily composed of brachiopods and trilobites (25–30%) (Fig. 8h; red arrows). The intraclasts (≤ 2 mm; poorly sorted, sub-angular to sub-rounded) (8–10%) are mainly composed of trilobites and small patches of dark micrite, or completely made up of mudstone (Fig. 8h; pink arrows). The ellipsoidal and round oncoids (10%; up to 1.5 mm in diameter) are characterized by well-laminated cortices (Fig. 8h; yellow arrows). These are similar to the Type C (concentrically arranged laminae) oncoids of Flügel (2010). Ooids (<10%; <1 mm) are usually moderately sorted. These ooids are partially neomorphosed (Fig. 8h; blue arrows) and composed of a random mosaic of sub-equant anhedral spar crystals.

Irregular intraclasts (Fig. 8h) indicate a highly hydrodynamic setting. The well-laminated and concentric cortices of oncoids (Fig. 8h) are characteristic of more-or-less persistent but moderate water movement and incrustation by cyanobacteria under comparatively high-energy conditions (Dahanayake, 1977). On the basis of the presence of grains such as broken skeletal fragments, ooids, a variety of poorly sorted muddy intraclasts, and slight micritization around grains, a shallow subtidal (leeward) shoal has been inferred as the depositional environment for this microfacies.

MF5: Ooid packstone (MF5) was observed in the Miaolingian Zhangxia Formation in Kelan and Qingshuihe sections. This microfacies is absent in the Furongian record in these sections and in the entire Cambrian record of the Kouquan section. The carbonate is cemented by micrite and mainly composed of ooid grains, intraclasts (<5%), and matrix, which appears to be dense, darkish brown lime mud (up to 25%) (Fig. 8i). One type of grain, i.e., radial-concentric ooids (0.3 mm to 1 mm), is predominant, with a possible bacterial biofilm at the core (Fig. 8i; yellow arrows). The composition of these ooids is the same in the center and the cortex. Dark micrite was observed in the cortex of a few of the ooids (Fig. 8i; red arrow heads).

This microfacies is mostly associated with radial-concentric ooids with cores of bacterial biofilm (Fig. 8i; Brehm et al., 2003, 2006). The concentric structure of these ooids indicates a high-energy setting. Moreover, the cortex of a few ooids consists of dark micrite which may point to the presence of filamentous cyanobacteria (*Girvanella*-type), further indicating the formation of these ooids under the influence of microbes in a microbial mat dominated by cyanobacteria (Liu and Zhang, 2012). The microfacies surrounded by micrite suggest a relatively moderate-energy setting, probably the leeward environment of a shoal (cf. Flügel, 2010; Riaz et al., 2022a).

MF6: Ooid grainstone (MF6) was observed in all stratigraphic sections. This is associated with up to 60% ooids and cemented with sparite cement (Fig. 8j). Radial-concentric ooids (with and without nuclei), composite ooids, and pseudo-ooids were identified (Fig. 8j). The composite ooids are composed of more than three sub-ooids, and their diameter depends on the number and size of the sub-ooids (Fig. 8j; green arrow). Neomorphosed ooids (Fig. 8j; blue arrows) were also recognized.

This microfacies indicates a high-energy environment, which can be easily proved from the concentric structure of the cortex, surrounded by sparry calcite, and by the matrix-free texture (grain-supported) (Fig. 8j; Flügel, 2010). The composite ooids developed with a dark, thin, organic envelope in a high-energy setting (Scholle and Ulmer-Scholle, 2003). Moreover, the neomorphosed ooids were most likely originally aragonitic in composition (Tucker, 1984; Tucker and Wright, 1990), and later underwent the dissolution of the aragonite and its replacement with calcite. The neomorphosed ooids may indicate highly turbulent conditions (Riaz et al., 2019a, 2021, 2022a).

MF7: Ooidal dolograinstone (MF7) was observed in the Zhangxia Formation (Kouquan section; Fig. 8k), the Fengshan Formation (Kelan section; Fig. 8l); and the Gushan Formation (Qingshuihe section; Fig. 8m). This microfacies is predominately characterized by oolitic grain-supported facies (Fig. 8k–m). The microfacies is associated with 60% ooids along with less than 10% dark micrite and pyrite minerals (Fig. 8k–m). The ooids of the Zhangxia Formation (Fig. 8k) include partially dolomitized ooids, whereas the Fengshan Formation (Fig. 8l) contains completely dolomitized ooids. The crystals of these completely dolomitized ooids range from 50 to 100 μm in size (Fig. 8l). Furthermore, pyrite minerals in the center and stylolite in the outer most cortex of the ooids from the Gushan Formation (Fig. 8m).

The partially dolomitized ooids in the Zhangxia (Fig. 8k) and Gushan formations (Fig. 8m) provide evidence for a high-energy setting due to concentric laminae and subaerial exposure resulting from partially dolomitized centers (Flügel, 2010). Moreover, the completely dolomitized ooids in the surrounding of connate cement confirms their formation in a high-energy setting above the fair-weather wave base (Burchette and Wright, 1992; Flügel, 2010). Furthermore, the partially dolomitized ooids of the Zhangxia Formation (Fig. 8k) represent the meteoric to shallow burial diagenetic environment (Khaing et al., 2022). Whereas completely dolomitized ooids of the Fengshan Formation (Fig. 8l) indicate the meteoric diagenesis (Khaing et al., 2022). Further partially and completely dolomitized carbonates are surrounded by blocky cement that also provide the evidences of meteoric diagenesis (Jafarian et al., 2017). The ooids of the Gushan Formation that contain the crystals of dolomite as well as stylolite (Fig. 8m) represent intermediate to deep burial diagenetic environment (Khaing et al., 2022).

MF8: Bioclast ooid grainstone (MF8) was observed in all sections and is associated with trilobites (Fig. 8n). These bioclasts also act as nuclei in several radial-concentric ooids (Fig. 8n). Furthermore, radial-concentric ooids without nuclei (Fig. 8n; yellow arrows) and neomorphosed ooids (Fig. 8n; blue arrows) were also observed in MF8. The radial-concentric ooids (0.6–1 mm) are larger in size than the neomorphosed ooids, which range from 0.3–0.5 mm in size (Fig. 8n). Moreover, dark micrite and pyrite grains (Fig. 8n; red dashed lines) were also observed in several places. Locally, MF8 can be merged into ooid bioclast grainstone to form packstone.

Trilobite fossils (Fig. 8n) were observed in abundance in Cambrian strata and indicate shallow shelf settings (Scholle and Ulmer-Scholle, 2003). The radial-concentric ooids with and without nuclei, as well as the predominance of their concentric fabric and the intense cementation by sparite (matrix-free grainstone), indicate a high-energy environment (Riaz et al., 2019a, 2022a). The central part of the radial-concentric ooids (without nuclei) is possibly associated with the calcification of bacterial biofilms (Brehm et al., 2003, 2006). Additionally, dark micrite in this microfacies is possibly associated with several microorganisms that may be actively involved in the formation of ooids (see Decho and Gutierrez, 2017; Dupraz et al., 2009). We suggest central to seaward shoal environments for this microfacies.

MF9: Ooid intraclast bioclast grainstone (MF9) was observed in the Furongian strata of all study sections. The bioclasts (<25%) are represented by fragments of brachiopods and/or trilobites (Fig. 8o). This microfacies also contains well-sorted ooids and elongated intraclasts (Fig. 8o; red arrows). These intraclasts (10%) mainly comprise small patches of dark micrite (Fig. 8o; red arrows). Quartz grains (Fig. 8o; blue arrow) and scattered dolomite particles (Fig. 8o; yellow arrows) were also recognized within the texture.

The fossils (Fig. 8o) indicate shallow shelf settings (Scholle and Ulmer-Scholle, 2003). Intraclasts point to the formation and destruction of sediments, which can be episodic and often repeated in storm-influenced coastal and shallow shelf settings (Flügel, 2010). These grains represent FZ5 and FZ6, i.e., platform margin sand shoals to the platform rim in Flügel's terms (Flügel, 2010). Additionally, crystals of dolomite were originally composed of calcite in which $Ca^{2+}$ was gradually replaced with $Mg^{2+}$. The dark and dense materials between the crystals of dolomite were possibly combined through EPS, mainly excreted by filamentous cyanobacteria (i.e., Dupraz et al., 2009; Decho, 2010; Decho and Gutierrez, 2017). Alternatively, these materials can also be explained by the accumulation of insoluble dusty material at the rim of crystals during secondary crystal growth (dolomite neomorphosis) (i.e., Barta, 2011).

### 4.3. Geochemical characterization of the Cambrian record

#### 4.3.1. SEM and EDX analyses

A number of analyses such as SEM and EDX were performed to explore the potential intrinsic association among the genesis of regressive carbonate deposits and their elemental composition. The SEM observations indicate the presence of exquisite features such as nanospheres, EPS, and microbial fossils within dark micrite (Fig. 9a–f). The dark micrite records two classes of microbial fossils, namely spherical and filamentous forms (Fig. 9a–c). The spherical microbial fossils have variable sizes of ~2.50 μm and rounded morphology (Fig. 9c), whereas the filamentous microbial fossils are 30–40 μm in length and 2–4 μm in diameter. Based on morphology, various forms of these fossils were identified, such as straight, intertwined, and unbranched (Fig. 9a, b). They also occur as tubular structures with no clear bifurcations (Fig. 9b), however, partial bifurcation was commonly recognized (Fig. 9b). The occurrence of EPS remnants inside the dark micrite, combined with filamentous fossils and nanospheres, was observed (Fig. 9c). The remnants of EPS indicate numerous lamellae having an irregular band with honeycomb surficial pore structures (Fig. 9c, e). The SEM images also show the rhombohedral morphology of calcite crystals (Fig. 9f). Qualitative elemental analyses (by EDX) were also conducted on filamentous microbial fossils (see EDX 001 in Fig. 9b), nanograin (EDX 002 in Fig. 9d), and EPS remnants (EDX 003 in Fig. 9e).

#### 4.3.2. Mineralogy

Petrographic and SEM investigations unraveled the close association of dark micrite with the genesis of Cambrian carbonate facies (Figs. 8, 9). To examine the formation of these facies, we investigated the geochemical signatures of these dark micrites by fluorescence microscopy and EPMA.

Fluorescence microscopic study supports the occurrence of dark micrite in the observed carbonate facies (Fig. 10a–g). Petrographic observations indicate the different natures of the ooids, including ooids with dominant nuclei as well as those without nuclei (Fig. 10b). The fluorescence study of these ooids also found the presence of obvious laminae in the ooids without nuclei and the conspicuous nuclei of bioclasts such as brachiopods or trilobite fragments in ooids with nuclei (Fig. 10c). In addition, the patches of dark micrite in the neighboring area of the ooids most likely reflects the preservation of organic matter remnants (Fig. 10b, c). Additionally, numerous ooids also display obvious concentric laminae that are not observable through microscopic study (Fig. 10d, e). Recently, Xiao et al. (2021) also reported cerebroid ooids in the Cambrian strata representing the presence of dark micrite (Fig. 10f, g).

An EPMA study was conducted to understand the chemistry of dark micrite in order to differentiate the micrite from the radial-concentric fibrous calcite. The targeted points of the EPMA are marked in Fig. 10b, d, f. (see yellow crosses numbered from 1 to 6). Their elemental composition is presented in Table 1. In particular, the results of the EPMA study confirm differences in the chemistry of dark micrite and radial-concentric fibrous calcite. Calcium (Ca), oxygen (O), and carbon (C) were almost majorly observed in both dark micrite and radial-concentric fibrous calcite. However, the concentration of the minor elements (i.e., Si, Al, Mg, N, K) in dark micrite is higher than in the radial-concentric fibrous calcite (Fig. 10; spectra 1 to 6). The key components of the studied ooids are Ca—Mg carbonates (calcite and Mg-calcite) (Fig. 10; Table 1).

#### 4.3.3. Isotopic records

The $\delta^{13}C$ and $\delta^{18}O$ isotopic analyses of eighty-one carbonate samples (Figs. 4, 11; Table 2) from the three different sections were used to interpret the geochemical records of the Cambrian strata. The isotopic values show variations in all studied sections of the NCP (Fig. 4; Table 2). The lower and uppermost parts of the Xuzhuang Formation (n: 5) at the Kelan section show negative $\delta^{13}C$ isotope values, whereas the middle-upper part of the formation exhibits positive $\delta^{13}C$ values (Table 2). Two samples have the highest negative $\delta^{18}O$ isotope values (i.e., −10.68‰ and −11.36‰ VPDB) of all the Xuzhuang samples (Fig. 4; Table 2). The mean values of $\delta^{13}C$ and $\delta^{18}O$ in the Xuzhuang Formation of the Kouquan and Qingshuihe sections are 0.02‰ and −8.15‰ VPDB, and −1.01‰ and − 8.59‰ VPDB, respectively (Table 2). In the Zhangxia Formation, $\delta^{13}C$ and $\delta^{18}O$ mean values are 0.3‰ and −8.17‰ (Kelan section), 0.16‰ and −9.49‰ (Kouquan section), and −0.01‰ and −7.85‰ (Qingshuihe section) (Fig. 4; Table 2). At the Kelan section, $\delta^{13}C$ values (mean = −0.5‰ VPDB) from the lower to the upper part of the Gushan Formation (n: 4) show a trend towards more negative values. The $\delta^{18}O$ values of these four samples range from −7.45‰ to −9.11‰ (mean = −8.2‰ VPDB). At the Kouquan section, the maximum and minimum $\delta^{13}C$ and $\delta^{18}O$ values of the Gushan Formation (n: 3) are 0.45‰ and −1.12‰ VPDB (mean = −0.26‰ VPDB), and −7.08‰ and −11.43‰ VPDB (mean = −9.12‰ VPDB), respectively, whereas the Gushan Formation (n: 4) at the Qingshuihe section comprises both negative and positive values of $\delta^{13}C$ (mean = −0.18‰ VPDB) (Fig. 4; Table 2). The mean value of the $\delta^{18}O$ at the Gushan Formation is −7.45‰ VPDB. The Furongian Changshan Formation (n: 4) at the Kelan section shows variations of $\delta^{13}C$ values similar to those in the Miaolingian strata (i.e., the Xuzhuang, Zhangxia, and Gushan formations) of the Kelan section (Figs. 4 and 11; Table 2). The Furongian Changshan Formation (n: 6) at the Kouquan section has only one sample that exhibits a $\delta^{13}C$ positive value (CS-17 = 0.46‰ VPDB), while other samples show negative $\delta^{13}C$ values varying between −0.05‰ and −0.54‰ VPDB (Table 2). The mean $\delta^{13}C$ and $\delta^{18}O$ values of the Changshan Formation are −0.14‰ and −7.74‰ VPDB, respectively. However, in the Changshan Formation (n: 5) at the Qingshuihe section all $\delta^{13}C$ values are negative, ranging between −0.13‰ and −0.69‰ VPDB (mean = −0.32‰ VPDB), and $\delta^{18}O$ values vary from −7.57‰

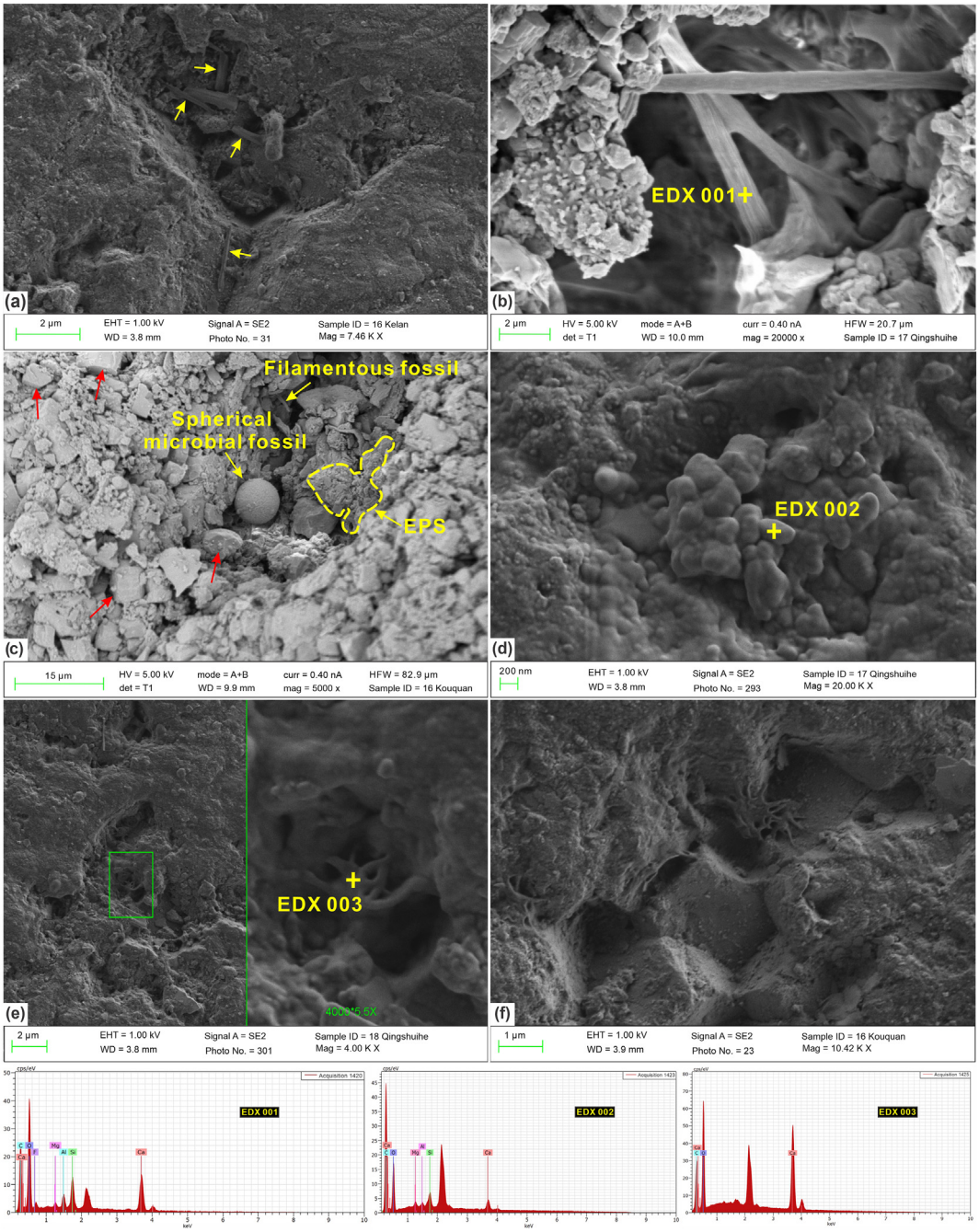


**Fig. 9.** Ultra-microfabrics of nanospheres, EPS calcified remnants, filamentous microbial fossils, and EDX spots. (a) Filamentous fossils having a calcified sheath of cyanobacteria (yellow arrow) are prominent within calcite crystal; (b) Filamentous fossils inside dark micrite indicating straight morphology, without bifurcation. Yellow cross displaying the target spot of EDX 001; (c) Spherical and filamentous microbial fossils, presence of calcite crystals (red arrows) and EPS calcified remnants; (d) Nanospheres agglomerated with EPS; yellow cross points out the target spot of EDX 002; (e) The green rectangle displays the EPS in dark micrite that noticeably confirm the EPS calcified remnants with irregular band-like shapes in zoom part; Yellow cross reveals the target spots of EDX 003; (f) Occurrence of rhombohedral shape calcite crystals.

to −9.47‰ VPDB (mean = −8.24‰ VPDB). The Fengshan Formation at the Kelan section exhibits entirely negative $\delta^{13}C$ values, whereas at the Kouquan section all $\delta^{13}C$ values are positive. On the other hand, $\delta^{13}C$ values in the Fengshan Formation at the Qingshuihe section are both positive and negative (Fig. 4; Table 2). The $\delta^{18}O$ values of the Fengshan Formation at the Kelan, Kouquan, and Qingshuihe sections range from −4.15‰ VPDB to −8.01‰ VPDB (mean = −6.22‰ VPDB; Table 2), −7.72‰ VPDB to −8.16‰ VPDB (mean = −7.96‰ VPDB; Table 2), and −4.55‰ to −8.42‰ VPDB (mean = −6‰ VPDB; Table 2), respectively.

## 5. Discussion

### 5.1. Depositional environment and sequence stratigraphy

Based on petrographic investigations, spatiotemporal trends and the variations of facies associations, the ooidal shoal in the middle Cambrian, and the bioherm limestone and calcirudites in the upper Cambrian, which points to sedimentation under the fair-weather wave base (FWWB), we suggest a deposition on a carbonate platform (probably a ramp) for the Cambrian NCP carbonates. The nine

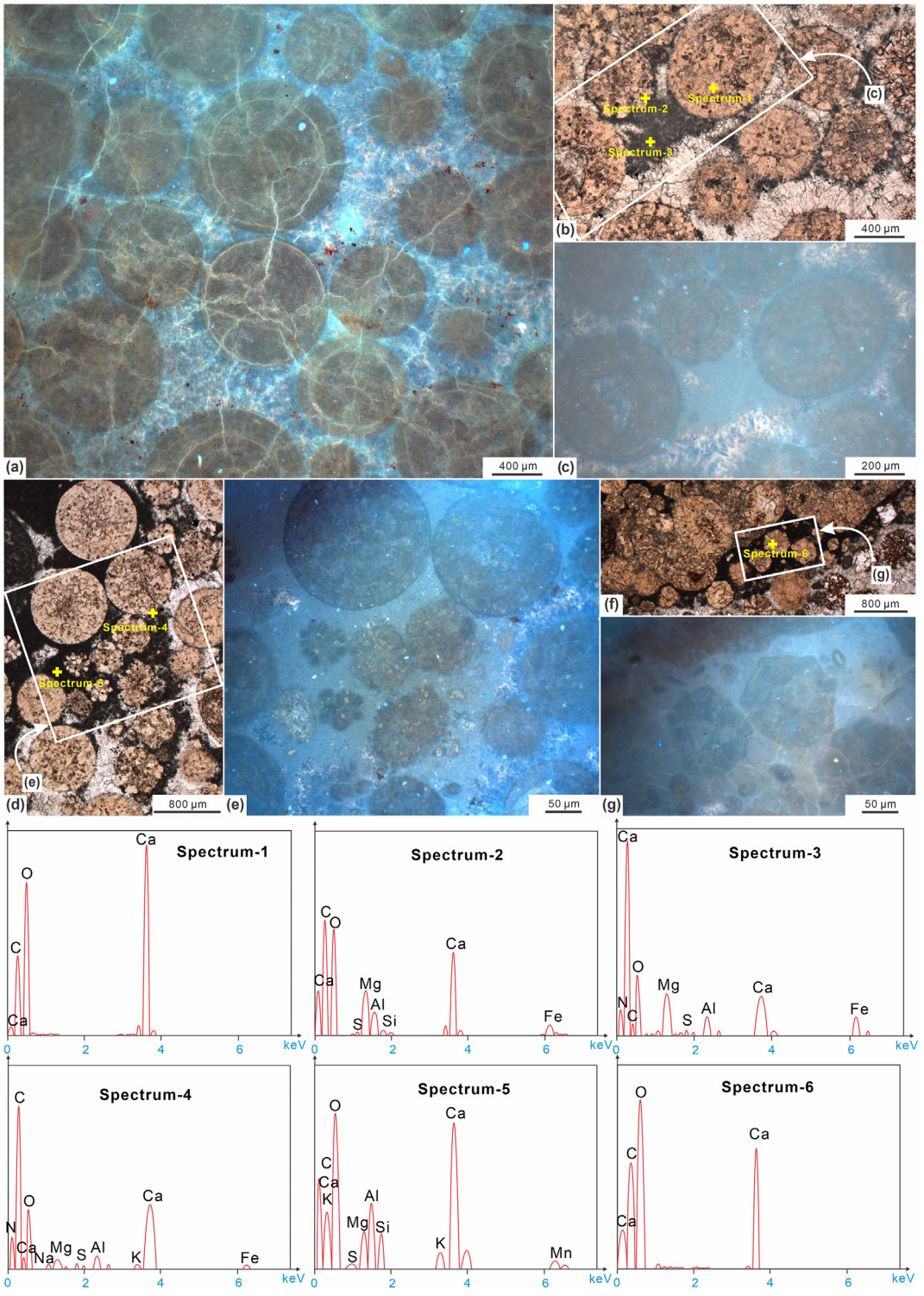


**Fig. 10.** Fluorescence photomicrographs, EPMA targets, and spectrum results of the carbonates at the NCP. (a) Fluorescence image indicates the radial-concentric structure; (b) Ooids and dark micrite within and surrounding area of the ooids; (c) Fluorescence image of ooids and dark micrite (rectangle in Fig. b); (d) Ooids without concentric laminae of micrite; (e) Fluorescence image of concentric laminae of dark micrite (square in Fig. d); (f) Classic ooids of the NCP are enclosed by dark micrite; (g) Fluorescence image of ooids (rectangle in Fig. f). The EPMA spectra are targeted on the photomicrographs b, d, and f. The data of targeted EPMA spots are reported in Table 1.

microfacies that have been identified in this study can be grouped into tidal flat, lagoon, and shoal facies associated with an inner ramp setting (Fig. 12).

The tidal flat comprises mudstone and microbial mudstone (MF1), and intraclast-bioclast wackestone-packstone (MF2), indicating that the facies trend from landward to seaward. In addition, this depositional environment of the microfacies points to the shallowness of a large body of this basin (Elicki et al., 2002; Alsharhan and Kendall, 2003; Flügel, 2010; Jafarian et al., 2017). The single identified lagoon microfacies (MF3) of the Cambrian carbonate ramp of North China is associated with peloid bioclast wackestone formed above the FWWB. The abundant occurrence of bioclasts points to normal-marine salinity (Flügel, 2010). The shoal facies associations suggest high-energy conditions comprising six microfacies (MF4–9) that are dominantly

**Table 1**
Element compositions of micrite and ooids from EPMA.

| Spectrum | Spectrum point location | Element compositions of micrite and ooids minerals | | | | | | | | | | | |
|---|---|---|---|---|---|---|---|---|---|---|---|---|---|
| | | $N_2O_5$ | $SiO_2$ | $SO_3$ | $CO_2$ | $Na_2O$ | MgO | $Al_2O_3$ | $K_2O$ | CaO | $MnO_2$ | FeO/FeS | Total |
| Spectrum 1 | Ooid (Fig. 10b) | | | | 45.86 | | | | | 52.32 | | | 98.18% |
| Spectrum 2 | Ooid (Fig. 10b) | | 0.32 | 0.27 | 53.47 | | 4.01 | 2.12 | | 35.10 | | 2.08 | 97.37% |
| Spectrum 3 | Micrite (Fig. 10b) | 0.43 | | 1.17 | 60.46 | | 4.13 | 3.16 | | 23.69 | | 4.02 | 97.06% |
| Spectrum 4 | Ooid (Fig. 10d) | 1.95 | | 0.42 | 59.30 | 0.55 | 1.27 | 2.18 | 0.30 | 32.38 | | 0.03 | 98.38% |
| Spectrum 5 | Micrite (Fig. 10d) | | 1.95 | | 49.01 | 0.16 | 4.15 | 5.40 | 0.23 | 38.34 | 0.06 | | 99.30% |
| Spectrum 6 | Ooid (Fig. 10f) | | | | 56.62 | | | | | 41.14 | | | 97.76% |

composed of ooids with minor oncoids, bioclasts, and intraclasts. Apart from this, shoal microfacies (i.e., MF7) comprises the meteoric and burial diagenetic environment. The petrographic interpretation defines the high abundance of shoal facies in the Cambrian Miaolingian strata of the NCP as have been deposited above the FWWB and within an inner ramp (shoal) environment (Fig. 12).

The field study revealed that the Cambrian (Miaolingian to Furongian) Xuzhuang, Zhangxia, Gushan, Changshan, and Fengshan formations at the Kelan, Kouquan, and Qingshuihe sections developed from retrogradational to progradational successions during fluctuations of relative sea level (Figs. 4–7). The studied Cambrian succession deposited during the first megasequence has some similarities and differences to the Cambrian strata in North America: a shale-carbonate lower part (shaly half-cycle) and a calcareous oolite-laminae upper part (carbonate half-cycle) (see Aitken, 1978; Chow and James, 1987). The shaly half-cycle can be interpreted as a highstand and the succeeding carbonate half-cycle as a lowstand (Osleger and Montafiez, 1996), a case similar to the two system tracts; a lower TST and upper HST have been interpreted from the studied sections of NCP. Moreover, the Cambrian strata of the NCP are composed of many meter-scale shallowing-upward cycles, just like the Cambrian strata of North America (Osleger and Read, 1991.). The studied calcareous mudstone, interbedded micritic limestone, and calcareous mudstone were part of the retrograding complex and developed during the rapid rise of relative sea level (Fig. 4) in a similar way to that described by Latif et al. (2018) and Riaz et al. (2019a, 2019b, 2022a). The shallow ramp and grain bank facies mostly associated with oolitic limestones, along with burrowing, scoured surfaces and cross-lamination, developed during progradation rather than aggradation (Figs. 4, 6b, c, f, g, i, 7b, d, e, f, i, 8h–n); this is evident due to high carbonate production and low-magnitude base level fall (i.e., shut down of carbonate factory), which causes slow sea-level fall, as described by Schlager and Warrlich (2009) and Mei (2010). The oolitic grainstone in the top part of each Miaolingian Formation (Figs. 4, 6b, c, f, 8i, j, k, m) is overlain by relatively deep-water calcareous mudstone of the same formation, fulfilling the regressive model of Mei and Yang (2000) and Samanta et al. (2016). The depositional style of the studied sections is almost similar to the eight other sections in the same provinces of China (Fig. 13; Riaz, 2019). These sections confirm that the oolitic grainstone in the upper part of each formation was covered by calcareous mudstone, providing evidence of transgression, whereas, the Furongian strata of these sections are comprised of carbonate mud (Fig. 13).

The Miaolingian strata (Xuzhuang, Zhangxia, and Gushan formations) developed supratidal flat deposits in the lower part of the Xuzhuang Formation, which represent the *platform initiation stage* as proposed by Mei et al. (1997) and Meng et al. (1997). The upper part of the formation predominantly consists of cross-laminated oolitic limestone (Figs. 6b, 7a) forming a shallow ramp subtidal-type meter-scale cycle (see Mei et al., 2005; Riaz et al., 2019a) and represents the *platform foundation stage* (e.g., Riaz et al., 2019b), whereas the middle part of the formation displays a condensed succession that represents the rapid rise of sea level (Baraboshkin, 2009) and separates the *platform initiation* and *platform foundation stages* (Fig. 5b) (Mei et al., 1997; Meng et al., 1997). Overall, the depositional style of the Xuzhuang Formation consists of a transgressive system tract plus a condensed section, and a highstand system tract (Figs. 4, 5b). A long-term relative sea level rise occurred during the deposition of the Xuzhuang Formation, as evidenced by the vast extension of the formation at the NCP (Xiao et al., 2017a, 2017b; Latif et al., 2018; Riaz et al., 2019a, 2019b). Subsequently, during normal regression, thick beds of oolitic limestone developed in shallow ramp settings (Ma et al., 2017; Riaz et al., 2019a, 2022a). The deposition of the Zhangxia Formation occurred in a shallow subtidal

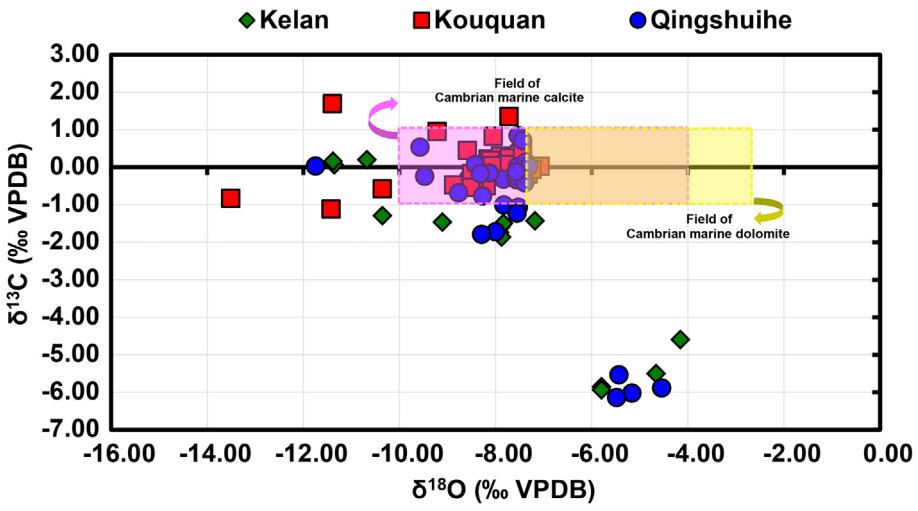


**Fig. 11.** Comparison of $\delta^{18}O$-$\delta^{13}C$ values of limestone and dolostone samples of the Cambrian of Kelan, Kouquan, and Qingshuihe sections with expected Cambrian marine dolomite and limestone (Veizer and Prokoph, 2015; Henkes et al., 2018; Ryb and Eiler, 2018).

**Table 2**
Values of carbon and oxygen isotopes along the studied section of the Cambrian strata of North China Platform.

| Formation | Kelan Section Shanxi Province | | | Kouquan Section Hebei Province | | | Qingshuihe Section Inner Mongolia | | |
|---|---|---|---|---|---|---|---|---|---|
| | Sample No. | δ13C (‰) VPDB | δ18O (‰) VPDB | Sample No. | δ13C (‰) VPDB | δ18O (‰) VPDB | Sample No. | δ13C (‰) VPDB | δ18O (‰) VPDB |
| Fengshan | FS-28 | −5.94 | −5.80 | FS-25 | 0.83 | −8.05 | FS-28 | −6.14 | −5.48 |
| | FS-27 | −4.60 | −4.15 | FS-24 | 0.22 | −8.16 | FS-27 | −6.02 | −5.16 |
| | FS-26 | −0.15 | −8.01 | FS-23 | 1.35 | −7.72 | FS-26 | −5.88 | −4.55 |
| | FS-25 | −0.03 | −7.62 | | | | FS-25 | 0.08 | −8.42 |
| | FS-24 | −0.20 | −7.79 | | | | FS-24 | −5.53 | −5.43 |
| | FS-23 | −5.51 | −4.66 | | | | | | |
| | FS-22 | −5.86 | −5.80 | | | | | | |
| Changshan | CS-21 | −1.30 | −10.36 | CS-22 | −0.49 | −8.20 | CS-23 | −0.69 | −8.77 |
| | CS-20 | 0.05 | −7.35 | CS-21 | −0.05 | −7.24 | CS-22 | −0.25 | −9.47 |
| | CS-19 | −0.08 | −7.45 | CS-20 | −0.19 | −7.32 | CS-21 | −0.13 | −7.57 |
| | CS-18 | 0.51 | −7.53 | CS-19 | −0.54 | −8.52 | CS-20 | −0.32 | −7.84 |
| | | | | CS-18 | −0.30 | −7.45 | CS-19 | −0.24 | −7.58 |
| | | | | CS-17 | 0.46 | −7.44 | | | |
| Gushan | GS-17 | −1.47 | −9.11 | GS-16 | 0.03 | −7.08 | GS-18 | 0.02 | −7.31 |
| | GS-16 | −0.20 | −8.55 | GS-15 | −1.12 | −11.43 | GS-17 | 0.02 | −7.54 |
| | GS-15 | −0.03 | −7.45 | GS-14 | 0.45 | −8.59 | GS-16 | −0.42 | −7.39 |
| | GS-14 | 0.06 | −7.57 | | | | GS-15 | −0.34 | −7.56 |
| Zhangxia | ZX-13 | 0.00 | −7.28 | ZX-13 | −0.17 | −8.50 | ZX-14 | 0.71 | −7.44 |
| | ZX-12 | 0.01 | −7.46 | ZX-12 | −0.47 | −8.87 | ZX-13 | 0.84 | −7.53 |
| | ZX-11 | 0.15 | −11.38 | ZX-11 | 0.96 | −9.22 | ZX-12 | −0.77 | −8.27 |
| | ZX-10 | −1.60 | −7.89 | ZX-10 | 0.07 | −7.77 | ZX-11 | −1.72 | −8.00 |
| | ZX-09 | −0.21 | −7.42 | ZX-09 | 1.70 | −11.40 | ZX-10 | 0.02 | −7.36 |
| | ZX-08 | −0.14 | −7.21 | ZX-08 | −0.58 | −10.36 | ZX-09 | 0.53 | −9.57 |
| | ZX-07 | −0.20 | −7.32 | ZX-07 | 0.25 | −7.72 | ZX-08 | 0.02 | −7.32 |
| | ZX-06 | −0.08 | −7.20 | ZX-06 | 0.05 | −8.07 | ZX-07 | 0.14 | −7.37 |
| | | | | ZX-05 | −0.83 | −13.51 | ZX-06 | 0.10 | −7.83 |
| Xuzhuang | XZ-05 | −1.86 | −7.87 | XZ-04 | 0.12 | −8.11 | XZ-05 | −1.79 | −8.29 |
| | XZ-04 | 0.06 | −11.36 | XZ-03 | −0.53 | −8.45 | XZ-04 | −1.07 | −7.53 |
| | XZ-03 | 0.20 | −10.68 | XZ-02 | 0.18 | −8.11 | XZ-03 | 0.04 | −11.75 |
| | XZ-02 | −0.07 | −7.84 | XZ-01 | 0.30 | −7.90 | XZ-02 | −1.01 | −7.83 |
| | XZ-01 | −1.74 | −7.91 | | | | XZ-01 | −1.23 | −7.56 |

setting during the Cambrian transgression (Mei and Mei, 1997). The lower part of the Zhangxia Formation represents a rapid transgression that directly covered the cross-laminated oolitic grainstone of the Xuzhuang Formation (Fig. 6a, b), whereas the upper part of the Zhangxia Formation is associated with the burrowed and scoured surface of oolitic grainstone (Figs. 6c, 7b) that represents the relative fall in sea level. In addition, the Cambrian transgression continued for longer and was more extensive than in the early and middle Miaolingian (Mei, 2011, 2015). This is the reason why calcirudites within calcareous mudstone produced a condensed section in the lower part of the Gushan Formation, indicating a rapid rise in sea level in the studied sections of the NCP (Fig. 6d, e). The lower part of the Gushan Formation directly covered the burrowed and scoured surfaces of the oolitic grainstone of the Zhangxia Formation (Fig. 7c), whereas the upper part of the formation displays a sharp contact with the Changshan Formation (Figs. 5d, 7g) that denotes Type III unconformity of drowning type (Schlager, 1989, 1999). The studied drowned unconformity (Fig. 7g) is different from the Exxon model for Type I and Type II sequence boundaries (Vail et al., 1984; Van Wagoner et al., 1990). The oolitic grainstone that starts in the upper part of the Xuzhuang Formation (Fig. 6b) and proceeds to the Zhangxia Formation (Fig. 6c) and the Gushan Formation (Fig. 6f) denotes the *platform foundation stage* (e.g., Mei et al., 1997). This *platform foundation stage* represents a carbonate platform that is dominated by oolitic shoals (Figs. 4, 6b, c, f,

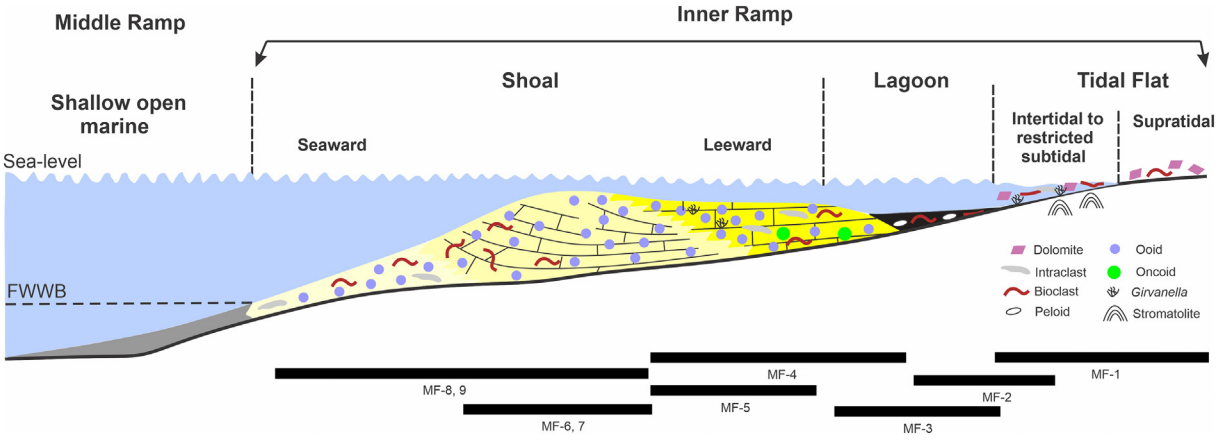


**Fig. 12.** Inferred depositional setting of the Cambrian strata of the studied sections. Note that the identified microfacies and microfacies associations were deposited above the fair-weather wave base (FWWB) and within an inner ramp environment.

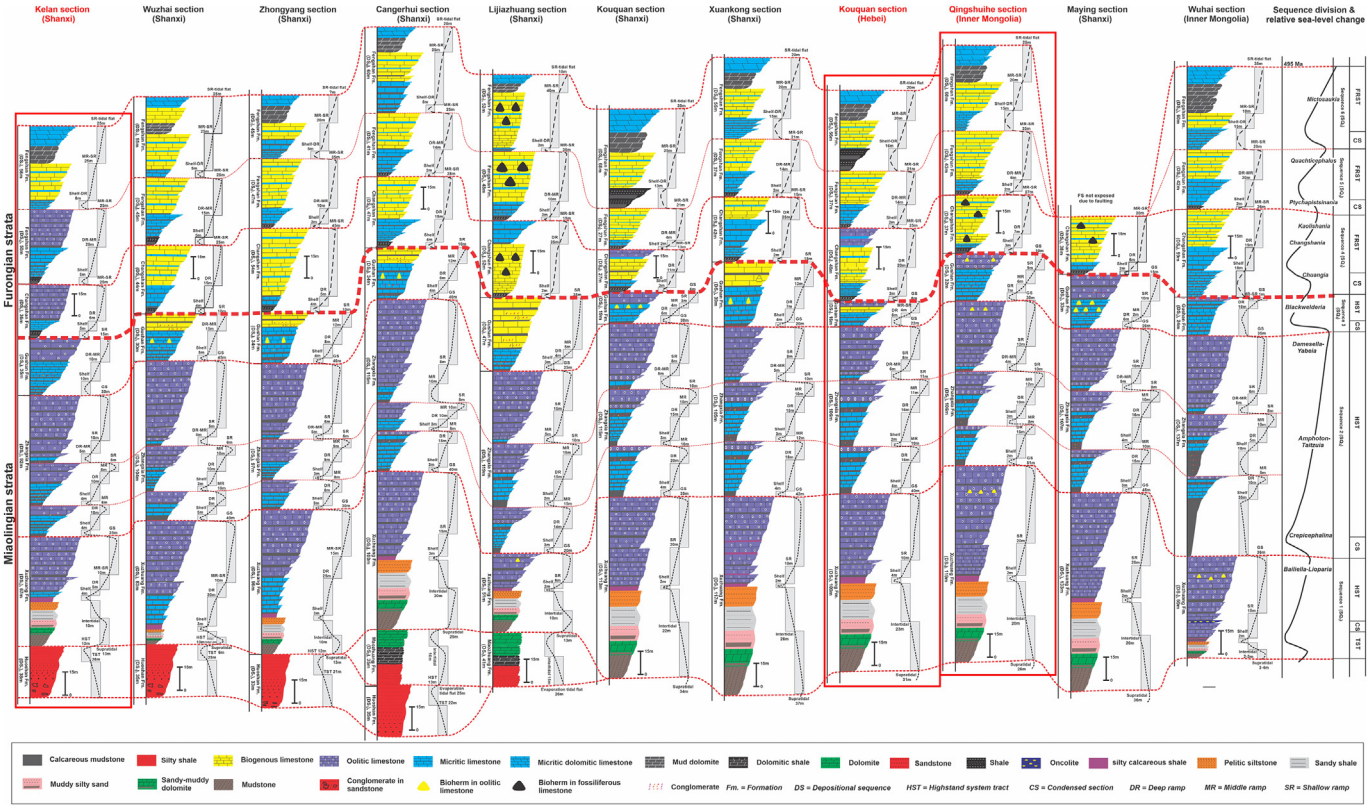


**Fig. 13.** The depositional style of the Cambrian strata at various sections of the studied provinces (i.e., Shanxi, Hebei, Inner Mongolia) of China (Adapted from Riaz, 2019).

13) and laid the foundation of a carbonate platform similar to the carbonate platform dominated by peloidal sands described by Pratt et al. (2012).

The Furongian strata (i.e., the Changshan and Fengshan formations) are composed of bored and burrowed fossiliferous limestone (Figs. 5f, 7i–j) and deposited in a relatively deeper environment than the Miaolingian strata, consisting of thick massive oolitic grainstone deposited in a shallow water high-energy environment (Riaz et al., 2019a). The Changshan Formation, which makes upper contact with the calcareous mudstone and shale of the basal part of the Fengshan Formation provides a typical example of the drowned unconformity (Fig. 7k) similar to the Miaolingian strata (Fig. 7g) of the studied sections of the NCP. The entire Furongian strata of the Kelan section deviates from fossiliferous limestone to oolitic-grain bank (Figs. 4, 13), which may have been caused by the platform drowning event at the end of the Cambrian Miaolingian Series (Ma et al., 2017; Riaz et al., 2019a). Further occurrence of the oolitic-grain bank in the Fengshan Formation at the Kelan section developed a high topography as compared to the other sections (e.g., Kouquan and Qingshuihe), thus providing a shallow-marine environment where an abundance of nutrient supply, microorganisms, possibly slightly elevated salinity, and development of concentric laminae as a result of turbulent water conditions were suitable agents for the formation of ooids.

### 5.2. Geochemical interpretations

Observations of the dark micrite in the NCP revealed exquisitely preserved structures such as microbial fossils, EPS calcification remnants, and nanospheres (Fig. 9a–f). The preserved structure of the dark micrite is composed of Ca, O, C, Mg, Si, Al, and F, as revealed by spot analyses by EDX (Fig. 9b, d, e) and confirmed by EPMA data (Fig. 10). Recently, Xiao et al. (2020a, 2020b) documented filamentous fossils and classified them into three varieties: 1) slightly bent filamentous fossils without bifurcation; 2) intertwined filamentous fossils, most likely products of the calcification of the passives sheathes of filamentous microorganisms; and 3) filamentous fossils without bending or bifurcation. A restricted portion of the Cambrian strata of the studied sections contains a third variety of filamentous fossils (Fig. 9a–b). EDX analysis of the microbial fossils revealed that the key compositional elements compositions are C and O (EDX 001 in Fig. 9b). Various elements including Ca, Mg, Si, Al, and F exist inside the filamentous fossils. Their main mineralogical composition includes calcite and clay minerals (EDX 001-003 in Fig. 9), reflecting the calcitic composition of carbonate facies in the Cambrian strata (Stanley, 2006).

In addition to the filamentous microbial fossils, spherical microbial fossils were also observed within the dark micrite of the carbonate facies (Fig. 9c). The geochemical data of Xiao et al. (2020a) indicate these fossils' bodies are predominantly comprised of calcite and clay minerals. The present work also reveals the presence of nanospheres, interpreted as the tiny grains precipitated on a cyanobacterial microbial mat (Fig. 9d). These grains show a close association with EPS due to the dual nature of EPS. We surmise that, initially, EPS in these observed nanospheres works as a “cation sponge” because of a negative group of amino acids (aspartic acid and glutamic acids) and carboxylated polysaccharides (uronic acids) that can prevent carbonate precipitation by excluding $Ca^{2+}$ from the solution (e.g., Decho and Gutierrez, 2017). Binding ability progressively declined owing to the presence of different microbes in the microbial mat. The further precipitation process was most likely promoted by biologically-induced mineralization in the carbonate grains of NCP, as argued by Dupraz et al. (2009). In addition, the composite mineralogical results of previous studies have also suggested that nanosphere aggregates denote products of the interface between heterotrophic bacteria metabolism and the degradation of EPSs (see Decho and Gutierrez, 2017; Diaz and Eberli, 2019), suggesting that a primary stage of biogenic carbonate particle nucleation was promoted by microbial metabolism (see Spadafor et al., 2010). The EDX interpretation consistently shows that the principal elements in the nanospheres

are Ca, C and O, suggesting that the mineralogical composition of these nanospheres is dominated by calcite (EDX 002 in Fig. 9d).

Besides the nanospheres, several fragmented sheets of EPS remnants were also documented around the filamentous microbial fossils (Fig. 9e). Extensive sheets of EPS remnants were observed inside the dark micrite, combined with nanospheres and filamentous microbial fossils (Fig. 9b, c, e). Close observations of these EPS lamellae demonstrated that their surfaces display an irregular band-like morphology as well as a honeycomb-like surficial pore structure (Fig. 9e). These features most likely reflect residual calcification of EPS, as argued by previous studies (e.g., Dupraz and Visscher, 2005; Dupraz et al., 2009). Their mineralogical investigation through EDX analysis further suggests that the EPS remnants with a typical structure are primarily composed of calcium carbonate and clay minerals (EDX 003 in Fig. 9e). Overall, the dark micrite reveals a large number of finely preserved microbial fossils and some microbially-related structures, including EPS calcification remnants and nanospheres (Fig. 9a–f). These signatures within the ooids further confirm their origin as a consequence of calcification products of microbial activity, which was significant in the Cambrian period (see Xiao et al., 2021).

Our EPMA data also suggest that the micrite is rich in elements such as Si, S, Na, K, Mn, Fe, N, and Al (Fig. 10, Table 1), although the micrite's major constituents are Ca, C, and O. The microzone at which N occurs is located inside the dark micrite closely associated with the studied ooids, indicating remnants of organic matter (see spectra 3 and 4). It is worth stating that our EPMA interpretation of dark micrite also reflects the occurrence of pyrite (framboidal), suggesting genesis under reducing conditions (Maclean et al., 2010; Xiao et al., 2020a). In conclusion, the integrated results EPMA and EDX for the elemental composition of dark micrite are in agreement with the tested lithification of microbial mats (see Farias et al., 2014; Zhu et al., 2018). Based on these findings, it can therefore be inferred that the dark micrite in the studied ooids supports its definition as calcified remnants of microbial mats composed of several microorganisms (Farias et al., 2014; Zhu et al., 2018).

In addition to the results from SEM-EDX and EPMA, our isotopic data also deliver reliable clues in favor of microbial involvement during the formation of the dark micrite in the studied ooids. Isotopic compositions across different study locations revealed a wide range of $\delta^{18}O$ values from −4.15 to −11.75‰ VPDB (Fig. 4; Table 2). In contrast, the $\delta^{13}C$ VPDB values indicate a range of −2 to +2‰ VPDB (Fig. 4; Table 2). The set of $\delta^{13}C$ values indicates similarity to the features of marine dissolved organic carbon (Campbell, 2006). Firstly, the negative values of $\delta^{13}C$ in the carbonate ooids imply that the carbon was primarily generated from a highly organic-rich zone, such as the microbial zone. Likewise, it can also be inferred that the depleted $^{13}C$ values of Cambrian ooids indicate that the carbon most likely originated from organic sources linked to the activity of sulphate-reducing bacteria (Figs. 4 and 11; Table 2; Warren, 2000). These $\delta^{13}C$ values of the carbonates facies depend on the relative content of $CO_2$, which was most probably provided via the disintegration of organic matter associated with the involvement of sulphate-reducing bacteria during cementation and recrystallization (e.g., Armstrong-Altrin et al., 2009). Moreover, we report that the $\delta^{13}C$ values of the Zhangxia Formation are greater than those of the Gushan Formation (see Table 2). This difference is highlighted by evidence, which suggests that the lower negative values of the carbon isotopes indicate that the genesis of the studied ooids was associated with microbial communities (as documented in the modern Bahamas; Diaz et al., 2013, 2015, 2017).

Many researchers have asserted that the negative $\delta^{18}O$ values of carbonate facies are promising indicators of meteoric influence or a high degree of recrystallization, which suggests that the original values were most probably affected by diagenetic alterations (e.g., Campbell, 2006; Campbell et al., 2008). The negative $\delta^{18}O$ values found in this study (see Table 2) are not consistent with marine water ambient temperature, but provide most promising support for diagenetic episodes (Fig. 11). Work by Veizer and Prokoph (2015) shows that the $\delta^{18}O$ values are more negative than those of modern seawater (from −6 to −8‰ VPDB), meaning that the $\delta^{18}O$ values observed in this study were mainly a result of marine-related diagenesis and little modification or alteration occurred during the burial processes. Slightly more depleted $\delta^{18}O$ values in some of the samples, in particular those from the Kelan and Kouquan sections, suggest either (i) recrystallization by pore waters/connate waters under burial conditions or (ii) an influence of temperature during burial processes that shifted the $\delta^{18}O$ values towards more negative values. Recent studies by Henkes et al. (2018) and Ryb and Eiler (2018) have used clumped isotopes to reconstruct the $\delta^{18}O$ values of the Phanerozoic and indicated that the $\delta^{18}O$ values of Cambrian seawater were very similar to those of modern seawater (0‰), or only slightly more negative (−2‰). If this is the case, the $\delta^{18}O$ values observed in all studied sections were heavily influenced by hot burial fluids, or the $\delta^{18}O$ values were modified by a geothermal gradient. The absence of pervasive burial diagenesis features in the studied samples, according to a study by Koeshidayatullah et al. (2020), show that the Cambrian seawater or marine calcite was more likely to have more negative $\delta^{18}O$ values than modern seawater (around −6‰), suggesting that a significant influence of burial fluids or geothermal gradient heating is highly unlikely. Therefore, the majority of the negative $\delta^{18}O$ values observed in the studied samples suggest the dominance of seawater diagenesis, whereas the more depleted $\delta^{18}O$ values observed in the Kelan and Kouquan sections can be attributed to cryptic burial recrystallization (Javanbakht et al., 2018).

Likewise, relatively strong depletion of $\delta^{13}C$ values compared to marine values (up to −6.2‰) in the Fengshan Formation at both the Kelan and Qingshuihe sections may indicate (i) the influence of meteoric diagenesis during subaerial exposure or (ii) carbon isotope negative excursion during Stage 10 in North China. Indeed, meteoric diagenesis would typically influence and shift both the $\delta^{13}C$ and $\delta^{18}O$ values towards more negative values, creating an inverted J-shaped curve (Allan and Matthews, 1982). This further supports the idea of negative $\delta^{13}C$ excursion during the diagenetic overprints.

## 6. Conclusions

(1) The Cambrian strata of the NCP indicate an epicontinental sea-type sedimentary succession that evolved on a low-latitude homoclinal ramp from the *platform initiation* to *platform foundation stage* of carbonate deposition during relative changes in sea level.

(2) We identified nine microfacies originating from three depositional environments, namely tidal flat, lagoon, and shoal areas that occurred on the inner part of a carbonate ramp. The shoal facies is the dominating facies type in the Miaolingian strata, developed during normal regression that fulfills the sequence stratigraphic model put forward by Schlager (2005). We propose that these shoal facies laid the foundation of a new ramp type of carbonate platform.

(3) Lithofacies such as calcareous mudstone, interbedded micritic limestone, and calcareous mudstone were deposited during transgressive system tract of third-order sequence, whereas scoured surfaces and cross-laminated oolitic grainstone were deposited during highstand system tract i.e., LHST of third-order sequence. The Cambrian strata are comprised of multiple episodes of platform submergence, indicating the development of typically drowned successions confined by five drowning unconformities, whereas the entire Cambrian strata is bounded at the top and bottom by Type I sequence boundaries of Exxon Model.

(4) The SEM analyses indicate nanospheres, EPS calcified remnants, and a considerable number of exquisite microbial fossils within the micrite, confirming that the micritic portion of the ooids represents the calcified remnants of microbial mats. This is further reinforced by the EPMA data, which suggest that the elemental compositions of micrites within or around the ooids are identical to those reported for lithomicrobial mats.

(5) Isotopic data also provide concrete evidence in favor of microbial involvement during the formation of Cambrian ooids. The $\delta^{18}O$ isotope values are more negative than those of modern seawater and most likely indicate marine-related diagenesis; little modification or alteration occurred during the burial processes while slightly more depleted $\delta^{18}O$ values in some of the samples endorse either recrystallization by connate waters under burial conditions or the influence of temperature during burial processes. Locally, a depletion in $\delta^{13}C$ values (of the Fengshan Formation) may reflect the influence of meteoric diagenesis.

## Data availability

Data will be made available on request.

## Declaration of competing interest

The authors declare that they have no competing financial interests or personal relationships that could have appeared to influence the work reported in this paper.

## Acknowledgments

This study was supported by National Natural Science Foundation of China (Grant No. 41472090). We are thankful to Professor Mei Mingxiang (China University of Geosciences Beijing), who helped us during the field work.

## References

Aitken, J.D., 1978. Revised model for depositional Grand Cycles, Cambrian of the southern Rocky Mountains, Canada. Bulletin of Canadian Petroleum Geology 26, 515–542.

Allan, J.R., Matthews, R.K., 1982. Isotope signatures associated with early meteoric diagenesis. Sedimentology 29, 797–817.

Alsharhan, A.S., Kendall, C.S.C., 2003. Holocene coastal carbonates and evaporites of the southern Arabian Gulf and their ancient analogues. Earth-Science Reviews 61 (3–4), 191–243.

Amel, H., Jafarian, A., Husinec, A., Koeshidayatullah, A., Swennen, R., 2015. Microfacies, depositional environment and diagenetic evolution controls on the reservoir quality of the Permian Upper Dalan Formation, Kish Gas Field. Marine and Petroleum Geology 67, 57–71.

Armstrong-Altrin, J.S., Lee, Y.I., Verma, S.P., Worden, R.H., 2009. Carbon, oxygen, and strontium isotope geochemistry of carbonate rocks of the Upper Miocene Kudankulam Formation, Southern India: Implications for paleoenvironment and diagenesis. Geochemistry 69 (1), 45–60.

Baraboshkin, E.Yu., 2009. Condensed sections: terminology, types, and accumulation conditions. Moscow University Geology Bulletin 64 (3), 153–160.

Barta, G., 2011. Secondary carbonates in loess-paleosoil sequences: a general review. Open Geosciences 3 (2), 129–146.

Batten, K.L., Narbonne, G.M., James, N.P., 2004. Paleoenvironments and growth of early Neoproterozoic calcimicrobial reefs: platformal Little Dal Group, northwestern Canada. Precambrian Research 133, 249–269.

Beigi, M., Jafarian, A., Javanbakht, M., Wanas, H., Mattern, F., Tabatabaei, A., 2017. Facies analysis, diagenesis and sequence stratigraphy of the carbonate-evaporite succession of the Upper Jurassic Surmeh Formation: impacts on reservoir quality (Salman oil field, Persian Gulf, Iran). Journal of African Earth Sciences 129, 179–194.

Bottjer, D.J., Hagadorn, J.W., Dornbos, S.Q., 2000. The Cambrian substrate revolution. GSA Today 10 (9), 1–7.

Brehm, U., Krumbein, W.E., Palinska, K.A., 2003. Microbial spheres: a novel cyanobacterial-diatom symbiosis. Naturwissenschaften 90, 136–140. https://doi.org/10.1007/s 00114-003-0403-x.

Brehm, U., Krumbein, W.E., Palinska, K.A., 2006. Biomicrospheres generate ooids in the Laboratory. Geomicrobiology Journal 23, 545–550.

Burchette, T.P., Wright, V.P., 1992. Carbonate ramp depositional systems. Sedimentary Geology 79, 3–57.

Campbell, K.A., 2006. Hydrocarbon seep and hydrothermal vent paleoenvironments and paleontology: past developments and future research directions. Palaeogeography, Palaeoclimatology, Palaeoecology 232, 362–407.

Campbell, K.A., Francis, D.A., Collins, M., Gregory, M.R., Nelson, C.S., Greinert, J., Aharon, P., 2008. Hydrocarbon seep-carbonates of a Miocene forearc (East Coast Basin), North Island, New Zealand. Sedimentary Geology 204, 83–105.

Chen, Z.-Q., Tu, C.Y., Pei, Y., Ogg, J., Fang, Y.H., Wu, S.Q., Feng, X.Q., Huang, Y.G., Guo, Z., Yang, H., 2019. Biosedimentological features of major microbe-metazoan transitions (MMTs) from Precambrian to Cenozoic. Earth-Science Reviews 189, 21–50.

Chow, N., James, N.P., 1987. Cambrian grand cycles: a northern Appalachian perspective. Geological Society of America Bulletin 98 (4), 418–429.

Collom, C.J., Johnston, P.A., Powell, W.G., 2009. Reinterpretation of 'Middle' Cambrian stratigraphy of the rifted western Laurentian margin: Burgess Shale Formation and contiguous units (Sauk II megasequence), Rocky Mountains, Canada. Palaeogeography, Palaeoclimatology, Palaeoecology 277 (1–2), 63–85.

Dahanayake, K., 1977. Classification of oncoids from the upper Jurassic carbonates of the French Jura. Sedimentary Geology 18 (4), 337–353.

Decho, A.W., 2010. Overview of biopolymer-induced mineralization: what goes on in biofilms? Ecological Engineering 36 (2), 137–144.

Decho, A.W., Gutierrez, T., 2017. Microbial extracellular polymeric substances (EPSs) in ocean systems. Frontiers in Microbiology 8, 922. https://doi.org/10.3389/fmicb.2017. 00922.

Diaz, M.R., Eberli, G.P., 2019. Decoding the mechanism of formation in marine ooids: a review. Earth-Science Reviews 190, 536–556.

Diaz, M.R., Piggot, A.M., Eberli, G.P., Klaus, J.S., 2013. Bacterial community of oolitic carbonate sediments of the Bahamas Archipelago. Marine Ecology Progress Series 485, 9–24.

Diaz, M.R., Swart, P.K., Eberli, G.P., Oehlert, A.M., Devlin, Q., Saied, A., Altabet, M.A., 2015. Geochemical evidence of microbial activity within ooids. Sedimentology 62, 2090–2112.

Diaz, M.R., Eberli, G.P., Blackwelder, P., Phillips, B., Swart, P.K., 2017. Microbially mediated organomineralization in the formation of ooids. The Geological Society of America 45 (9), 771–774.

DiBenedetto, S., Grotzinger, J., 2005. Geomorphic evolution of a storm dominated carbonate ramp (c. 549 Ma), Nama Group, Namibia. Geological Magazine 142, 583–604.

Dupraz, C., Visscher, P.T., 2005. Microbial lithification in marine stromatolites and hypersaline mats. Trends in Microbiology 13 (9), 429–438.

Dupraz, C., Reid, R.P., Braissant, O., Decho, A.W., Norman, R.S., Visscher, P.T., 2009. Processes of carbonate precipitation in modern microbial mats. Earth-Science Reviews 96 (3), 141–162.

Elicki, O., Schneider, J., Shinaq, R., 2002. Prominent facies from the lower/Middle Cambrian of the Dead Sea area (Jordan) and their palaeodepositional significance. Bulletin de la Societé géologique de France 173 (6), 547–552.

Farias, M.E., Contreras, M., Rasuk, M.C., Kurth, D., Flores, M.R., Poiré, D.G., Novoa, F., Visscher, P.T., 2014. Characterization of bacterial diversity associated with microbial mats, gypsum evaporites and carbonate microbialites in thalassic wetlands: Tebenquiche and La Brava, Salar de Atacama, Chile. Extremophiles 18 (2), 311–329.

Feng, Z., Wang, Y., Zhang, J., Zuo, W., Zhang, X., Hong, G., Chen, J., Wu, S., Chen, Y., Chi, Y., Yang, C., 1990. Lithofacies Paleogeography of the Early Paleozoic of North China Platform. Petroleum Industry Press, Beijing, pp. 28–48 (in Chinese).

Feng, Z.Z., Peng, Y.M., Jin, Z.K., Jiang, P.L., Bao, Z.D., 2004. Lithofacies Palaeogeography of the Cambrian and Ordovician in China. Petroleum Industry Press, Beijing, pp. 112–121 (in Chinese).

Flügel, E., 2010. Microfacies of Carbonate Rocks: Analysis, Interpretation and Application. 2nd edition. Springer-Verlag, Berlin.

Henkes, G.A., Passey, B.H., Grossman, E.L., Shenton, B.J., Yancey, T.E., Perez-Huerta, A., 2018. Temperature evolution and the oxygen isotope composition of Phanerozoic oceans from carbonate clumped isotope thermometry. Earth and Planetary Science Letters 490, 40–50.

Ivantsov, A.Y., Zhuravlev, A.Y., Leguta, A.V., Krassilov, V.A., Melnikova, L.M., Ushatinskaya, G.T., 2005. Palaeoecology of the early Cambrian Sinsk biota from the Siberian platform. Palaeogeography, Palaeoclimatology, Palaeoecology 220 (1–2), 69–88.

Jafarian, A., Fallah-Bagtash, R., Mattern, F., Heubeck, C., 2017. Reservoir quality along a homoclinal carbonate ramp deposit: the Permian Upper Dalan Formation, South Pars Field, Persian Gulf Basin. Marine and Petroleum Geology 88, 587–604.

Javanbakht, M., Wanas, H., Jafarian, A., Shahsavan, N., Sahraeyan, M., 2018. Carbonate diagenesis in the Barremian-Aptian Tirgan Formation (Kopet-Dagh Basin, NE Iran): petrographic, geochemical and reservoir quality constraints. Journal of African Earth Sciences 144, 122–135.

Khaing, K.K., Latif, K., Oo, T.H., Hussein, A.A.A., Aung, M.M., Mei, C.J., 2022. Diagenetic implications for the oolitic limestone in the Miaolingian Zhangxia Formation, Beijing (North China Platform). Carbonates and Evaporites 37 (67). https://doi.org/10.1007/s13146-022-00808-y.

Koeshidayatullah, A., Corlett, H., Stacey, J., Swart, P.K., Boyce, A., Robertson, H., Whitaker, F., Hollis, C., 2020. Evaluating new fault-controlled hydrothermal dolomitization models: insights from the Cambrian Dolomite, Western Canadian Sedimentary Basin. Sedimentology 67 (6), 2945–2973.

Latif, K., Xiao, E.Z., Riaz, M., Wang, L., Khan, M.Y., Hussein, A.A., Khan, M.U., 2018. Sequence stratigraphy, sea-level changes and depositional systems in the Cambrian of the North China Platform: a case study of Kouquan section, Shanxi Province, China. Journal of Himalayan Earth Sciences 51, 1–16.

Latif, K., Xiao, E.Z., Riaz, M., Hussein, A.A.A., 2019. Calcified cyanobacteria fossils from the leiolitic bioherm in the Furongian Changshan Formation, Datong (North China Platform). Carbonates and Evaporites 34, 825–843.

Lee, H.S., Chough, S.K., 2006. Lithostratigraphy and depositional environments of the Pyeongan Supergroup (Carboniferous–Permian) in the Taebaek area, mid-East Korea. Journal of Asian Earth Sciences 26, 339–352.

Liu, W., Zhang, X.L., 2012. *Girvanella*-coated grains from Cambrian oolitic limestone. Facies 58 (4), 779–787.

Lu, Y.H., Zhang, W.T., Zhu, Z.L., Zhou, Z.Y., Yuan, J.L., Peng, S.C., Qian, Y., Zhang, S.G., 1994. Suggestions for the establishment of the Cambrian Stages in China. Journal of Stratigrapphy 18 (4), 318–328 (in Chinese with English abstract).

Lv, D., Chen, J., 2014. Depositional environments and sequence stratigraphy of the Late Carboniferous–Early Permian coal-bearing successions (Shandong Province, China):

sequence development in an epicontinental basin. Journal of Asian Earth Sciences 79, 16–30.
Ma, Y.S., Mei, M.X., Zhou, R.X., Yang, W., 2017. Forming patterns for the oolitic bank within the sequence-stratigraphic framework: an example from the Cambrian Series 3 at the Xiaweidian section in the Western Suburb of Beijing. Acta Petrologica Sinica 33 (4), 1021–1036 (in Chinese with English abstract).
Maclean, L.C., Tyliszczak, T., Gilbert, P.U., Zhou, D., Pray, T.J., Onstott, T.C., Shoutham, G., 2010. A high-resolution chemical and structural study of framboidal pyrite formed within a low-temperature bacterial biofilm. Geobiology 6 (5), 471–480.
Magaritz, M., Holser, W.T., Kirschvink, J.L., 1986. Carbon-isotope events across the Precambrian/Cambrian boundary on the Siberian Platform. Nature 320 (6059), 258–259.
Mei, M.X., 1993. Genetic types of the carbonate meter-scale cycles and their discerning marks. Sedimentary Facies and Palaeogeography 13 (6), 34–45 (in Chinese with English abstract).
Mei, M.X., 2010. Correlation of sequence boundaries according to discerning between normal and forced regressions: the first advance in sequence stratigraphy. Journal of Paleogeography 12 (5), 549–564 (in Chinese with English abstarct).
Mei, M.X., 2011. Depositional trends and sequence-stratigraphic successions under the Cambrian second-order transgressive setting in the North China Platform: a case study of the Xiaweidian section in the western suburb of Beijing. Geology of China 38 (2), 317–337 (in Chinese).
Mei, M.X., 2015. An important new progress in sequence stratigraphy from sedimentary sequence to sea-level change sequence-sequence stratigraphy. Journal of Stratigraphy 39 (1), 58–73 (in Chinese).
Mei, M.X., Mei, S.L., 1997. Cyclic-sequences of Composite Sea-level Change developed in Zhangxia Formation of Middle-Cambrian in North-China. Acta Sedimentologica Sinica 15 (4), 5–10 (in Chinese with English abstract).
Mei, M.X., Yang, X.D., 2000. Forced regression and forced regressive wedge system tract: revision on traditional exxon model of sequence stratigraphy. Geological Science and Technology Information 19 (2), 17–21 (in Chinese with English abstract).
Mei, M.X., Ma, Y.S., Mei, S.L., Hu, J.Z., 1997. Sequence-stratigraphic framework and carbonate-platform evolution for the Cambrian of the North-China Platform. Geoscience 11 (3), 275–282 (in Chinese with English abstract).
Mei, M.X., Xu, D., Zhou, H., 2000. Genetic types of meter-scale sequences and their fabric natures of facies succession. Journal of Earth Science 11 (4), 375–382.
Mei, M.X., Ma, Y.S., Deng, J., Chen, H.J., 2005. From cycles to sequences: sequence stratigraphy and relative sea level changes for the late Cambrian of the North China Platform. Acta Geologica Sinica 79 (3), 372–383.
Mei, M.X., Latif, K., Mei, C.J., Gao, J., Meng, Q.F., 2020a. Thrombolitic clots dominated by filamentous cyanobacteria and crusts of radio-fibrous calcite in the Furongian Changshan Formation, North China. Sedimentary Geology https://doi.org/10.1016/j.sedgeo.2019. 105540.
Mei, C.J., Riaz, M., Wang, L., Latif, K., Zhang, R., 2020b. Development of Middle Cambrian leiolitic bioherms dominated by calcified microbes: a case study of the Xinji Section (North China Platform). Marine Micropaleontology https://doi.org/10.1016/j.marmicro. 2020.101858.
Mei, M.X., Riaz, M., Zhang, Z.W., Meng, Q.F., Hu, Y., 2021. Diversified calcimicrobes in dendrolites of the Zhangxia Formation, Miaolingian Series (Middle Cambrian) of the North China craton. Journal of Palaeogeography 10 (8). https://doi.org/10.1186/s42501-021-00087-z.
Meng, X.H., Qiao, X.F., Ge, M., 1986. Study on ancient shallow sea carbonate storm deposits (tempestite) in North China and Dingjiatan model of facies sequences. Acta Sedimentologica Sinica 4 (2), 1–18 (in Chinese with English abstract).
Meng, X.H., Ge, M., Tucker, M.E., 1997. Sequence stratigraphy, sea-level changes and depositional systems in the Cambro-Ordovician of the North China carbonate platform. Sedimentary Geology 114 (1–4), 189–222.
Meyerhoff, A.A., Kamen-Kaye, M., Chen, C., Taner, I., 1991. China—Stratigraphy, Paleogeography, and Tectonics. Kluwer Academic Publishers, Dordrecht, Netherlands (188 pp.).
Montanez, I.P., Osleger, D.A., 1993. Parasequence Stacking Patterns, Third-Order Accommodation Events, and Sequence Stratigraphy of Middle to Upper Cambrian Platform Carbonates, Bonanza King Formation, Southern Great Basin: Chapter 12. pp. 305–326.
Myrow, P.M., Tice, L., Archuleta, B., Clark, B., Taylor, J.F., Ripperdan, R.L., 2004. Flat-pebble conglomerate: its multiple origins and relationship to metre-scale depositional cycles. Sedimentology 51, 973–996.
Myrow, P.M., Chen, J., Snyder, Z., Leslie, S., Fike, D.A., Fanning, C.M., Yuan, J., Tang, P., 2015. Depositional history, tectonics, and provenance of the Cambrian-Ordovician succession in the western margin of the North China block. Geological Society of America Bulletin 127, 1174–1193.
Osleger, D., Montafiez, I.P., 1996. Cross-platform architecture of a sequence boundary in mixed siliciclastic-carbonate lithofacies, Middle Cambrian, southern Great Basin, USA. Sedimentology 43, 197–217.
Osleger, D., Read, J.E., 1991. Relation of eustasy to stacking patterns of metre-scale carbonate cycles, late Cambrian, U.S.A. Journal of Sedimentary Research 61, 1225–1252.
Pan, B., Skovsted, C.B., Sun, H., Li, G., 2019. Biostratigraphical and palaeogeographical implications of Early Cambrian hyoliths from the North China Platform. Alcheringa: An Australasian Journal of Palaeontology 43 (3), 351–380.
Peng, S.C., 2009. Review on the studies of Cambrian trilobite faunas from Jiangnan slope belt, South China, with notes on Cambrian correlation between south and North China. Acta Palaeontologica Sinica 48, 437–452 (in Chinese with English abstract).
Peng, S.C., Zhao, Y.L., 2018. The proposed global standard stratotype-section and point (GSSP) for the conterminous base of Miaolingian series and Wuliuan stage at Balang, Jianhe, Guizhou, China was ratified by IUGS. Journal of Stratigraphy 42, 325–327 (in Chinese without English abstract).
Peng, S.C., Babcock, L.E., Cooper, R.A., 2012. The Cambrian Period (chapter 19). In: Gradstein, F.M., Ogg, J.G., Schmitz, M.D., Ogg, G.M. (Eds.), The Geologic Time Scale 2012. Elsevier, Amsterdam, pp. 437–488.
Peters, S.E., Gaines, R.R., 2012. Formation of the 'Great Unconformity' as a trigger for the Cambrian explosion. Nature 484, 363–366.
Pomar, L., Hallock, P., 2008. Carbonate factories: a conundrum in sedimentary geology. Earth-Science Reviews 87 (3–4), 134–169.
Pratt, B.R., Raviolo, M.M., Bordonaro, O.L., 2012. Carbonate platform dominated by peloidal sands: lower Ordovician La Silla Formation of the eastern Precordillera, San Juan, Argentina. Sedimentology 59, 843–866.
Pruss, S.B., Finnegan, S., Fischer, W.W., Knoll, A.H., 2010. Carbonates in skeleton-poor seas: new insights from Cambrian and Ordovician strata of Laurentia. Palaios 25, 73–84.
Riaz, M., 2019. Integrated Sedimentology and Sequence Stratigraphy of the Cambrian Ooids in the North China Platform. (PhD Thesis)China University of Geosciences, Beijing.
Riaz, M., Xiao, E.Z., Latif, K., Zafar, T., 2019a. Sequence-stratigraphic position of oolitic bank of Cambrian in North China Platform: example from the Kelan section of Shanxi province. Arabian Journal for Science and Engineering 44, 391–407.
Riaz, M., Latif, K., Zafar, T., Xiao, E.Z., Ghazi, S., Wang, L., Hussein, A.A., 2019b. Assessment of Cambrian Sequence Stratigraphic style of the North China Platform exposed in Wuhai division, Inner Mongolia. Himalayan Geology 40 (1), 92–102.
Riaz, M., Zafar, T., Latif, K., Ghazi, S., Xiao, E.Z., 2020. Petrographic and rare earth elemental characteristics of Cambrian *Girvanella* oncoids exposed in the North China Platform: constraints on forming mechanism, REE sources, and paleoenvironments. Arabian Journal of Geosciences https://doi.org/10.1007/s12517-020-05750-8.
Riaz, M., Zafar, T., Latif, K., Ghazi, S., Xiao, E.Z., 2021. Cambrian ooids, their genesis and relationship to sea-level rise and fall: a case study of the Qingshuihe section, Inner Mongolia, China. Stratigraphy 18 (2), 139–151.
Riaz, M., Bhat, G.M., Latif, K., Zafar, T., Ghazi, S., 2022a. Sequence stratigraphy, depositional and diagenetic environments of the Late Cambrian glauconite bearing oolitic limestones in the Kelan Section, Shanxi, China. Journal of Earth System Science 131 (17). https://doi.org/10.1007/s12040-021-01743-7.
Riaz, M., Latif, K., Zafar, T., Xiao, E.Z., Ghazi, S., 2022b. Morphology and genesis of the Cambrian oncoids in Wuhai Section, Inner Mongolia, China. Carbonates and Evaporites https://doi.org/10.1007/s13146-021-00750-5.
Riding, R., 2011. Calcified cyanobacteria. In: Reitner, J., Thiel, V. (Eds.), Encyclopedia of Geobiology. Springer, Heidelberg, pp. 211–223.
Rowland, S.M., Shapiro, R.S., 2002. Reef patterns and environmental influences in the Cambrian and earliest Ordovician. In: Kiessling, W., Flügel, E., Golonka, J. (Eds.), Phanerozoic Reef Patterns. SEPM Special Publicationvol. 72, pp. 95–128.
Ryb, U., Eiler, J.M., 2018. Oxygen isotope composition of the Phanerozoic Ocean and a possible solution to the dolomite problem. Proceedings of the National Academy of Sciences 115 (26), 6602–6607.
Samanta, P., Mukhopadhyay, S., Eriksson, P.G., 2016. Forced regressive wedge in the Mesoproterozoic Koldaha shale, Vindhyan basin, Son Valley, central India. Marine and Petroleum Geology 71, 329–343.
Schlager, W., 1989. Drowning unconformities on carbonate platforms. In: Crevello, P.D., Wilson, J.L., Sarg, J.F., Read, J.F. (Eds.), Controls on Carbonate Platform and Basin Development. SEPM Special Publication, Houston, pp. 15–25.
Schlager, W., 1999. Type 3 sequence boundaries. In: Harris, P.M., Saller, A.H., Simo, J.A. (Eds.), Advances in Carbonate Sequence Stratigraphy: Application to Reservoirs, Outcrop, and Models. SEPM Special Publication, Houston, pp. 35–46.
Schlager, W., 2003. Benthic carbonate factories of the Phanerozoic. International Journal of Earth Sciences 92 (4), 445–464.
Schlager, W., 2005. Carbonate Sedimentology and Sequence Stratigraphy. SEPM Concepts in Sedimentology and Paleontologyvol. 8. SEPM, Tulsa, Oklahoma (200 pp.).
Schlager, W., Warrlich, G., 2009. Record of sea-level fall in tropical carbonates. Basin Research 21, 209–224.
Scholle, P.A., Ulmer-Scholle, D.S., 2003. A color guide to the petrography of carbonate rocks: grains, textures, porosity, diagenesis. American Association of Petroleum Geologist. Memoir 77 (474 pp.).
Sepkoski, J.J., 1997. Biodiversity: past, present, and future. Journal of Paleontology 71 (4), 533–539.
Spadafor, A., Perri, E., Mckenzie, J.A., Vasconcelos, C., 2010. Microbial biomineralization processes forming modern Ca: Mg carbonate stromatolites. Sedimentology 57, 27–40.
Sperling, E.A., Stockey, R.G., 2018. The temporal and environmental context of early animal evolution: considering all the ingredients of an "explosion". Integrative and Comparative Biology 58, 605–622.
Stanley, S.M., 2006. Influence of seawater chemistry on biomineralization throughout Phanerozoic time: Paleontological and experimental evidence. Palaeogeography, Palaeoclimatology, Palaeoecology 232 (2–4), 214–236.
Swart, P., 2015. The geochemistry of carbonate diagenesis: the past, present and future. Sedimentology 62, 1233–1304.
Theisen, C.H., Sumner, D.Y., 2016. Thrombolite fabrics and origins: in fluences of diverse microbial and metazoan processes on Cambrian thrombolite variability in the Great Basin, California and Nevada. Sedimentology 63, 2217–2252.
Tucker, M.E., 1984. Calcitic, aragonitic and mixed calcitic-aragonitic ooids from the mid-Proterozoic Belt Supergroup, Montana. Sedimentology 31 (5), 627–644.
Tucker, M.E., Wright, V.P., 1990. Carbonate Sedimentology. Blackwell Science, Oxford, p. 482.
Vail, P.R., Hardenbol, J., Todd, R.G., 1984. Jurassic unconformities, chronostratigraphy and sea-level changes from seismic stratigraphy and biostratigraphy. In: Schlee, J.S. (Ed.), Interregional Unconformities and Hydrocarbon Exploration. American Association of Petroleum Geologist Memoir, pp. 129–144.
Van Wagoner, J.C., Mitchum Jr., R.M., Campion, K.M., Rahmanian, V.D., 1990. Siliciclastic Sequence Stratigraphy in Well Logs, Core, and Outcrops: Concepts for High-Resolution Correlation of Time and Facies. American Association of Petroleum Geologists Methods in Exploration Seriesvol. 7 (55 pp.).

Veizer, J., Prokoph, A., 2015. Temperatures and oxygen isotopic composition of Phanerozoic oceans. Earth-Science Reviews 146, 92–104.
Vickers-Rich, P., Komarower, P., 2007. The Rise and Fall of the Ediacaran Biota. Geological Society of London.
Wang, C.S., Fan, K.Q., Yin, Z.G., 1990. Features of ooids in the Middle Cambrian Zhangxia Formation in the Western Hills, Beijing, and their environmental significance. Bulletin of the Chinese Academy of Geological Science 22, 39–55 (in Chinese).
Wang, H.Z., Shi, X.Y., Wang, X.L., Yin, H.F., Qiao, X.F., Liu, B.P., Li, S.T., Chen, J.Q., 2000. Research on the Sequence Stratigraphy of China. Guangdong Science and Technology Press, Guangzhou (457 pp.) (in Chinese).
Warren, J., 2000. Dolomite: occurrence, evolution and economically important associations. Earth-Science Reviews 52, 1–81.
Wood, R., Liu, A.G., Bowyer, F., Wilby, P.R., Dunn, F.S., Kenchington, C.G., Cuthill, J.F.H., Mitchell, E.G., Penny, A., 2019. Integrated records of environmental change and evolution challenge the Cambrian Explosion. Nature ecology & evolution 3 (4), 528–538.
Xiang, L.W., Zhu, Z.l., Li, S.J., Zhou, Z.Q., 1999. Stratigraphical Lexicon of China (Cambrian). Geological Publishing House, Beijing (95 pp.) (in Chinese).
Xiao, E.Z., Qin, Y., Riaz, M., Latif, K., Yao, L., Wang, H., 2017a. Sequence stratigraphy division of Cambrian in the northeast area of Lvliang Mountain: a case study of the Cangerhui section in Wenshui City. Journal of Northeast Petroleum University 41 (5), 43–53.
Xiao, E.Z., Sui, M., Qing, Y., Latif, K., Riaz, M., Wang, H., 2017b. Cambrian sequence stratigraphic division for Qijiayu section in Hebei Laiyuan. Petroleum Geology and Oilfield Development in Daqing 36 (6), 16–25.
Xiao, E.Z., Zafar, T., Latif, K., Riaz, M., Lu, Y., 2020a. Geochemical and petrographic analyses of the Cambrian oncoids of the North China Platform: Implications for their paleogeography and paleoenvironment. Arabian Journal for Science and Engineering https://doi.org/10.1007/s13369-019-04146-5.
Xiao, E.Z., Latif, K., Riaz, M., 2020b. The genetic implications of microbial fossils for microbial carbonate: an example of Cambrian in North China Platform. Himalayan Geology 41 (2), 183–194.
Xiao, E.Z., Riaz, M., Zafar, T., Latif, K., 2021. Cambrian marine radial cerebroid ooids: Participatory products of microbial processes. Geological Journal 56 (9), 4627–4644.
Zhang, X., Shu, D., 2021. Current understanding on the Cambrian Explosion: questions and answers. PalZ 1–20. https://doi.org/10.1007/s12542-021-00568-5.
Zhang, X., Zhang, N., Yang, Z.H., Bao, Z.Y., Xia, W.C., 2009. Carbonate microfacies and sedimentary facies of Middle Cambrian Formation at Xiaweidian profile in Western Hills, Beijing, China. Geological Science and Technology Information 28 (6), 25–30 (in Chinese with English abstract).
Zhu, T.T., Lin, Y.C., Lu, X.C., Dittrich, M., 2018. Assessment of cyanobacterial species for carbonate precipitation on mortar surface under different conditions. Ecological Engineering 120, 154–163.